Direct Numerical Simulations of Intrusive Density- and Particle-Driven Gravity Currents

EP Francisco[1], LFR Espath[2,*], S Laizet[3], JH Silvestrini[4], VM Calo[5]

School of Engineering, Ftec, Porto Alegre-RS, Brazil,
School of Mathematical Sciences, University of Nottingham, Nottingham, NG7 2RD, United Kingdom,
Imperial College London,
Pontifical Catholic University of Rio Grande do Sul (PUCRS),
Curtin University, Bentley, Perth, Western Australia, Australia

Abstract

In the present study, mesopycnal flows are investigated using Direct Numerical Simulations (DNS). In particular, intrusive density- and particle-driven gravity currents in the lock exchange set-up are simulated with the high-order finite-difference framework `Xcompact3d`. To account for the settling velocity of particles, a customised Fick's law for the particle-solution species is used with an additional term incorporating a constant settling velocity proportional to the concentration of particles. A general energy budget equation is presented, for which the energy can migrate across the domain's boundaries. The relevant main features of intrusive gravity currents, such as front velocity, energy exchanges, sedimentation rate, deposit profile, and deposit map are discussed with comparison between two and three-dimensional simulations. In particular, the influence of the Grashof number, the interface thickness, the energy exchanges, the sedimentation process, and how the presence of more than one particle fraction may change the flow dynamics are investigated. The results are in good agreement with previous experiments and theoretical work, in particular for the prediction of the front velocity. For the particle-driven case, the suspended mass evolution along with the sedimentation rate suggests the occurrence of three different stages. In the first stage after the lock release, the particle mixture tends to suspend itself due to gravitational forces. Once most of the particle-mixture mass is suspended, the current intrudes while increases its velocity, reaching its kinetic energy peak. In the last stage, the particles are deposited at a nearly constant sedimentation rate. As a results, the front velocity constantly decelerates.

Keywords: Intrusive particle-driven gravity current, Direct numerical simulation, Fingering instability

1. Introduction

Gravity currents can be generated experimentally or numerically by the removal of a vertical lock gate separating two fluids of different densities at rest. An idealized set-up is when the two fluids are in a horizontal (or inclined) channel, with a constant or stratified density for the ambient fluid (He et al., 2021;

*Corresponding author.
Email address: `espath@gmail.com` (LFR Espath)
[1]School of Engineering, Ftec, Porto Alegre-RS, Brazil
[2]School of Mathematical Sciences, University of Nottingham, Nottingham, NG7 2RD, United Kingdom
[3]Turbulence, Mixing and Flow Control Group, Department of Aeronautics, Imperial College London, London SW7 2AZ, United Kingdom
[4]School of Engineering, Pontifical Catholic University of Rio Grande do Sul, Av. Ipiranga 6681, 90619-900 Porto Alegre-RS, Brazil
[5]School of Electrical Engineering, Computing and Mathematical Sciences, Curtin University, P.O. Box U1987, Perth, WA 6845, Australia

Biegert et al., 2017). Gravity currents in the lock-exchange set-up can be classified according to the effect of buoyancy, i.e., hyperpycnal, mesopycnal, or hypopycnal flows: hyperpycnal flows account for negative buoyancy that propagate as underflows, hypopycnal flows have a positive buoyancy and are overflows. When the density of the fluid in the lock is between the minimum and maximum densities of the ambient fluid, the gravity current will propagate in the form of an intrusion current at a level where the density of the fluid in the lock is comparable to the densities of the ambient (mesopycnal gravity currents). Hyperpycnal and hypopycnal currents have been extensively studied in the literature while mesopycnal gravity currents have received less attention from the scientific community with only a small number of numerical, theoretical and experimental studies, see Monaghan (2007); Ungarish (2009); White and Helfrich (2012) for an introduction on mesopycnal gravity currents.

Laboratory experiments were carried out in Rooij et al. (1999) in the lock-exchange set-up for a fixed volume of saline and particle laden fluid into a two-layer stratification. An integral model was developed by the authors and compared with their experiments. The model describes the time-evolution of the length of the intrusion and the sediment distribution it produces and was found to be in good agreement with the experimental data. Laboratory experiments using shadowgraph and particle tracking methods were performed in Lowe et al. (2002) for intrusive gravity currents in the lock-exchange set-up. The authors reported that the flow inside the intrusive current can be divided into three regions: an energy-conserving head region where the fluid velocity is nearly uniform with speed equal to the front speed, a dissipative wake region where large billows are present enhancing mixing with the ambient, with a non-uniform velocity approximately 50% greater than the front speed, and a tail region with very little mixing and a uniform velocity slightly faster than the front speed.

The dynamics of a gravity current that propagates along the interface of a two-layer fluid was studied experimentally in Sutherland et al. (2004) for a symmetric case (in which the upper- and lower-layer depth of the ambient are equal and the density of the intrusion is the average density of the ambient) and for an asymmetric case circumstances in which the density of the intrusion differs from the mean density of the ambient and in which the upper- and lower-layer fluid depths are unequal. Theoretical expressions to predict the speed and vertical extent of the gravity current head were compared with laboratory experiments. The authors found an excellent agreement between the theory and the experiments if the density of the gravity current is the average of the upper- and lower-layer densities weighted by the respective depths of the two layers. They also reported a significantly underprediction of the the gravity current speeds if the current density differs from this weighted-mean average. The discrepancy was attributed to the generation of waves that lead and trail the gravity current head. Rectilinear and radially spreading intrusive gravity currents were studied numerically in Ungarish (2005) using a closed one-layer shallow-water inviscid formulation and 2D DNS. It was found that the shallow-water model is able to predict the main features of an intrusive gravity current in particular, the initial propagation with a constant velocity for a rectilinear lock, the effect of the shape of the lock on the fluid motion and the spreading rate of the current. Excellent agreement with experiments was obtained for this simplified model.

An experimental and numerical study of an intrusion propagating along the interface of a two-layer fluid in a lock-exchange set-up was presented in Cheong et al. (2006). It was found that if the layer depths in the ambient are equal, the speed of the intrusion is independent of the density of the intrusion. Using 2D Direct Numerical Simulations, the authors found a good agreement with their experiments for the temporal evolution of the intrusive current. They also developed an energy model to describe the variation of the intrusion speed as a function of the intrusion and layer densities and the ratio of the layer depths. Rectilinear and radially spreading intrusive gravity currents were studied experimentally and with 2D DNS in Sutherland and Nault (2007). The authors found that intrusive currents at a finite-depth interface propagate at constant speed even when the head height decreases and that they can propagate without decelerating for very long distance, for several lock lengths in a rectilinear geometry and beyond several lock radii in an axisymmetric geometry. Both experiments and DNS demonstrated that the intrusion speed decreases to half the two-layer speed when the interface spans the lock-exchange set-up.

The formation, evolution, and structure of intrusive Boussinesq gravity currents propagating into a two-layer fluid with a sharp interface were investigated using highly resolved large eddy simulation (LES) in Ooi et al. (2007). It was found that the LES are in good agreement with experimental and theoretical work. A

mathematical model to study high Reynolds number, quasi-steady, intrusive gravity currents propagating into a two-layer ambient fluid was developed in Nokes et al. (2008). The model was based on inviscid, irrotational flow theory, and was used to predict the speed of the intrusive current as a function of its head height. The model was compared with the results obtained from two sets of experimental data. It was found that the model was able to capture accurately the evolution of the intrusive current and that the mixing and dissipation that occur behind the head seem to have a negligible impact of the speed of the current.

An analytical, experimental and numerical study of gravity currents propagating through a two-layer stratified ambient of finite vertical extent in the lock-exchange set-up was presented in Tan et al. (2011); Flynn et al. (2012). In particular, the authors focused on studying supercritical gravity currents where the Froude number is larger than 1. One of the main results of these studies is that the front speed is essentially independent of the interface thickness, at least for the range of parameters considered in this study. Overall the proposed models, based on a one-layer shallow-water approximation and designed to be derived without reliance on adjustable constants and ad hoc closures was reported to be a simple and versatile tools to study the main features of intrusive gravity currents. Vorticity-based models were developed in Khodkar et al. (2016, 2018) for intrusive gravity currents propagating along the interface of a two-layer stratified ambient. The models are based on the conservation of mass and vorticity and do not require any empirical closure assumptions. A parametric study performed with these models demonstrated their ability to reproduce the behaviour of intrusive currents, consistently with previous experimental observations. Specifically, these models can predict the formation of equilibrium intrusions when the intrusion density equals the depth-weighted mean density of the two ambient layers. The authors also used 2D DNS to back up their models and found very good agreement between the vorticity-based models and the 2D simulations.

Lock-release gravity current experiments were performed in Sutherland et al. (2018) to examine the evolution of a particle bearing flow that propagates either in a uniform-density fluid or in a two-layer fluid. A key result from this study for mesopycnal currents is that, in a two-layer fluid, the current was found to reverse direction as a consequence of the rise of interstitial fluid from the top layer ambient fluid and the particles from the bottom layer ambient fluid.

In this work, Boussinesq intrusive gravity currents in a two-layer ambient fluid are investigated with 2D and 3D DNS. Density and particle-driven gravity currents are considered thanks to a new framework to account for the settling velocity of particles. The new framework is based on an evolution of Fick's law for the particle-solution species with an additional term incorporating a constant settling velocity proportional to the concentration of particles. Furthermore, a general energy budget derived from the Navier-Stokes equations is used to study the energy transfers when the intrusive current is propagating into the two-layer ambient fluid. This energy budget can account for energy losses due to internal work and energy exchanges through the boundaries. The main features of the current such as as front velocity, energy exchanges, sedimentation rate, deposit profile, and deposit map are presented and compared with reference data. In particular, the simulations were designed to match the experimental set-up of Sutherland et al. (2004). The focus of the present study is on the influence of the Grashof number, the interface thickness, the energy exchanges, the sedimentation process, and how the presence of more than one particle fraction may change the flow dynamics.

The manuscript is organized as follows. Section 2 describes the assumptions that allow us to define the system of conservation equations describing the process and the constitutive assumptions to describe the physical response of the mixture system. Section 3 introduces the dimensionless form of the resulting system of equations and specifies the boundary conditions to uniquely define a solution. In this section, we also describe the setup of the highly-resolved numerical experiments we perform, detailing the initial conditions for both the density- and particle-driven cases. In section 4, we present the numerical experiments that allow us to study the influence of the Grashof number (Gr), the interface thickness and the presence of various particle fractions that may change the flow dynamics and the energy exchanges that control the sedimentation process. Finally, Section 5 describes our contributions.

2. General Governing Equations and Constitutive Equations

The incompressible Navier–Stokes equations under the Boussinesq assumption are used in the present study to describe the dynamics of the flow (particle erosion and re-suspension are neglected) . The balance laws in their dimensional form can be expressed as follows. The linear momentum equation is given by the Navier–Stokes equations augmented by the Boussinesq buoyancy body force

$$\rho\left[\frac{\partial \mathbf{v}}{\partial t}+\operatorname{div}(\mathbf{v}\otimes\mathbf{v})\right]-\operatorname{div}\mathbf{T}-[\![\rho]\!]g\mathbf{e}^{g}=\mathbf{0}, \tag{1}$$

where ρ, $\mathbf{v}$, and $[\![\rho]\!]\mathbf{e}^{g}$ are respectively the density, velocity, and body force due to the density difference in the two-layer ambient fluid. In the body force, $[\![\rho]\!]$ represents the density difference and $\mathbf{e}^{g}$ is a unit vector pointing in the direction of gravity. In the Boussinesq approximation, the density difference should be small enough (below 5%). The Cauchy stress tensor is defined as $\mathbf{T}=\mathbf{T}^{visc}-p\mathbf{I}$, where $\mathbf{T}^{visc}$ is the viscous stress, $\mathbf{I}$ the identity tensor, and p the pressure. Moreover, for incompressible fluids, the mass equation reads

$$\operatorname{div}\mathbf{v}=0. \tag{2}$$

For the particle and salinity concentrations, the following mass transfer equations are used

$$\frac{\partial \phi_a^{part}}{\partial t}+\operatorname{div}(\phi_a^{part}\mathbf{v})+\operatorname{div}\mathbf{j}_a^{part}=0,\quad a=1,\ldots,n_s, \tag{3}$$

and

$$\frac{\partial \phi^{salt}}{\partial t}+\operatorname{div}(\phi^{salt}\mathbf{v})+\operatorname{div}\mathbf{j}^{salt}=0. \tag{4}$$

Here, the superscript (part) and (salt) refer to the particles and salinity species. The suspended particles may have different granulometries, characterized by their volume fraction. Also, ϕ and $\mathbf{j}$ are the volume fractions and their diffusive mass flux, respectively. As a consequence, it is required to solve one transport equation for each particle fraction, where n_s is the total number of different particle diameters. The first and second order tensors are denoted by by bold lower and upper case symbols, respectively. The differential operators $\operatorname{grad}(\cdot)$, $\operatorname{div}(\cdot)$, $\operatorname{curl}(\cdot)$ represent the gradient, divergence and curl operators, respectively. The superscript $(\cdot)^{\top}$ denotes the transpose and $\otimes$ the tensor (dyadic) product.

The viscous stress tensor $\mathbf{T}^{visc}$ in an incompressible Newtonian fluid linearly dependent on the strain rate tensor $\mathbf{D}$, and is expressed as

$$\mathbf{T}^{visc}=2\mu\mathbf{D}\quad\text{where}\quad\mathbf{D}=\frac{1}{2}\left((\operatorname{grad}\mathbf{v})^{\top}+\operatorname{grad}\mathbf{v}\right), \tag{5}$$

where μ is the dynamic viscosity.

The constitutive equation for the particle-water and salt-water mass fluxes are as follows, based on the assumption that the fluxes do not interact, which is a customary assumption if cross-diffusion coefficients are unknown. In this setting, for the flux of particle concentrations, a modified Fick's law is used with a constant flux due to the particle settling velocity

$$\begin{aligned}\mathbf{j}_a^{part}=\quad & -\kappa_a^{part}\operatorname{grad}\phi_a^{part}+\phi_a^{part}\mathbf{v}_a^{s},\\ & a=1,\ldots,n_s^{part},\quad\text{no sum on } a,\end{aligned} \tag{6}$$

while for the salinity concentration, we employ the classical Fick's law

$$\mathbf{j}^{salt}=-\kappa^{salt}\operatorname{grad}\phi^{salt}, \tag{7}$$

where κ_i^{part} and κ^{salt} are the mass diffusivity coefficients for the different particles and salinity species, respectively. $\mathbf{v}_a^{s}=u_a^{s}\mathbf{e}^{g}$ is the a-th settling velocity of the particles $(0,-u_a^{s},0)$. The settling velocity is related to the particle diameter by the Stokes settling velocity law (for more details on this relation, the interested reader is referred to Julien (1998, 2010)). Note also that the diffusion coefficients are constant.

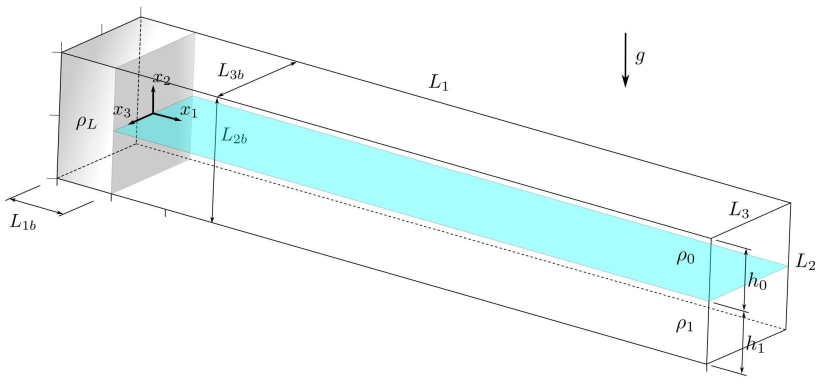

Figure 1: Sketch of the computational domain. The horizontal cyan plane delimits the interface between the two ambient fluids and the left box is the initial lock.

3. Numerical Methods and Parameters

The lock-release apparatus and domain characteristics are introduced in this section to make the governing equations dimensionless. Figure 1 shows the domain and the density configurations ρ_L, ρ_0, and ρ_1. The cyan plane in Figure 1 defines the interface between the two-layer ambient fluid with different densities ρ_0 and ρ_1, whereas the density of the fluid in the lock is ρ_L. The heights of these layers are denoted by h_1 and h_0. The total length, height and width of the lock-release apparatus are $(L_1, L_2, L_3) = (9.833, 1, 1)$, respectively, while the lock along the streamwise direction is L_{1b}. In the proposed simulations, the lock lengths in the spanwise L_{2b} and streamwise L_{3b} directions are equal to the domain dimensions in those directions, respectively, $L_{2b} = L_2$ and $L_{3b} = L_3$. The axes (x_1, x_2, x_3) are defined along the streamwise, vertical and spanwise direction, respectively.

To make these equations dimensionless, the entire box height $h = L_2$, which is equal to $h_0 + h_1$, is chosen as the characteristic length scale and the buoyancy velocity u_b as the characteristic velocity scale. The reduced gravitational acceleration defines the buoyancy velocity as $u_b = \sqrt{g'h}$ where $g' = (\llbracket\rho\rrbracket/\rho_1)g$, and g the gravitational acceleration. The Grashof number is $Gr = (u_b h/\nu)^2$ where $\nu = \mu/\rho$ is the kinematic viscosity. Another important dimensionless number that will appear later is the Schmidt number, defined as $Sc = \nu/\kappa$, where κ is the mass diffusivity of the particle-fluid mixture or salinity. Although the Froude number does not appear explicitly in the governing equations, it plays a central role. The Froude number equals the dimensionless front velocity $Fr = v_f$, which in turn is made dimensionless with the buoyancy velocity. For this study, all other variables are made dimensionless using ϕ_a^{part}, ϕ^{salt}, h or/and u_b. Thus, the linear momentum equation (1) can be expressed as

$$\frac{\partial \mathbf{v}}{\partial t} + \mathbf{v} \cdot \operatorname{grad} \mathbf{v} - \operatorname{div} \mathbf{T} - b_\rho \, \mathbf{e}^g = \mathbf{0}, \tag{8}$$

with

$$\mathbf{T} = \frac{2}{\sqrt{Gr}} \mathbf{D} - p\mathbf{I}. \tag{9}$$

Within the Boussinesq's assumption, the buoyancy force due to the density excess may be written as $b_\rho = \alpha_0 \phi^{salt} + \sum_{a=1}^{n_s} \alpha_a \phi_a^{part}$, where, in the general case, the coefficients α represent the relative weight among the concentrations. For density-driven cases, this buoyancy force is defined by $b_\rho = \alpha_0 \phi^{salt}$ with $\alpha_0 = 2$, whereas for the particle-driven cases, $b_\rho = \alpha_0 \phi^{salt} + \sum_{a=1}^{n_{part}} \alpha_a \phi_a^{part}$ with $\alpha_0 = 2$ and $\alpha_a = 1$ for all $1 \leq a \leq n_{part}$. For the mono-disperse particle-driven cases, $\alpha_0 = 2$, $\alpha_1 = 1$, and for the poly-disperse particle-driven case $\alpha_0 = 2$, $\alpha_1 = 1$, and $\alpha_2 = 1$.

By setting $\alpha_0 = 2$ instead of 1, the reduced gravity g' is twice as great as the reduced gravity found in Sutherland et al. (2004); Ooi et al. (2007); An et al. (2012). As a result of this choice, the buoyancy velocity

u_b, the Froude and Grashof numbers are scaled by $\sqrt{2}$ and time is scaled by $1/\sqrt{2}$. This rescaling is needed to compare the present results with the reference data of Sutherland et al. (2004); Ooi et al. (2007); An et al. (2012).

The mass equation (2) in the dimensionless form keeps the same structure

$$\operatorname{div} \mathbf{v} = 0, \tag{10}$$

while the equations for the particle concentrations (3) can be expressed as

$$\frac{\partial \phi_a^{part}}{\partial t} + \mathbf{v} \cdot \operatorname{grad} \phi_a^{part} + \operatorname{div} \mathbf{j}_a^{part} = 0, \tag{11}$$

with

$$\begin{aligned} \mathbf{j}_a^{part} = \quad & -\frac{1}{\sqrt{Gr(Sc_a^{part})^2}} \operatorname{grad} \phi_a^{part} + \phi_a^{part} \mathbf{v}_a^s, \\ & a = 1, \ldots, n_s^{part}, \quad \text{no sum on } a. \end{aligned} \tag{12}$$

(12) represents a modified Fick's law with a constant diffusion of particles in the vertical direction proportional to the particle fraction to emulate the settling process. Conversely, Necker et al. (2005) incorporated a linear advective term directly in the equation of the particle concentration. In the present approach, natural boundary conditions, namely Neumann boundary conditions for the mass fluxes, arise naturally, that is, the Fick's law for the particle-solution species is modified with an additional term incorporating a constant settling velocity proportional to the concentration of particles. This approach allows us to provide natural boundary conditions in a traditional manner, by assigning the normal component of the flux.

In a similar fashion, the equation for the salinity concentration (4) can be expressed as

$$\frac{\partial \phi^{salt}}{\partial t} + \mathbf{v} \cdot \operatorname{grad} \phi^{salt} + \operatorname{div} \mathbf{j}^{salt} = 0, \tag{13}$$

with (7) taking the form

$$\mathbf{j}^{salt} = -\frac{1}{\sqrt{Gr(Sc^{salt})^2}} \operatorname{grad} \phi^{salt}. \tag{14}$$

3.1. Boundary Conditions

To mimic free-surface boundary conditions for the velocity field at the top of the domain, a free-slip condition is used as follow, $\frac{\partial v_1}{\partial x_2} = \frac{\partial v_3}{\partial x_2} = 0$ with $v_2 = 0$ (no fluid can leave the computational domain). At the bottom of the computational domain, left- and right-end walls of the channel (see Figure 1), no-slip boundary condition are used. For the 3D simulations, free-slip and no-penetration boundary conditions are employed in the spanwise direction.

To emulate the sedimentation process of particles while neglecting erosion/re-suspension, an outflow boundary condition is used at the bottom wall for the particle concentration. It is based on a linear advection equation with a constant advective velocity, equal to the settling velocity,

$$\begin{aligned} \frac{\partial \phi_a^{part}}{\partial t} + \mathbf{v}_a^s \cdot \operatorname{grad} \phi_a^{part} \quad & = 0, \\ & a = 1, \ldots, n_s^{part}, \quad \text{no sum on } a. \end{aligned} \tag{15}$$

For the other boundary conditions (except the bottom wall) a no-flux condition $\mathbf{j}_a^{part} \cdot \mathbf{n} = 0$ is used, in dimensionless form, to obtain

$$\left(-\frac{1}{\sqrt{Gr(Sc_a^{part})^2}} \text{grad}\, \phi_a^{part} + \mathbf{v}_a^s \phi_a^{part} \right) \cdot \mathbf{n} = 0,$$
$$a = 1, \ldots, n_s^{part}, \quad \text{no sum on } a, \tag{16}$$

where $\mathbf{n}$ is the outer unit normal vector. Given the form of the mass flux $\mathbf{j}_a^{part}$ in expression (12), the boundary condition in (16) can be seen as a general form of the boundary conditions proposed in Necker et al. (2005). Finally, as for the salinity concentration, no-flux boundary conditions are used everywhere, that is, $\mathbf{j}^{salt} \cdot \mathbf{n} = 0$.

3.2. Initial conditions: density- and particle-driven gravity currents

The main parameters of the eleven (11) simulations presented in this work can be found in Table 1. Five of them are intrusive density-driven gravity currents, while the other six are intrusive particle-driven gravity currents. As for the density-driven cases, four simulations (cases $\#1 - 4.2\text{D}$) are 2D and one simulation (case #2.3D) is 3D. As for the particle-driven cases, four simulations (cases $\#5 - 8.2\text{D}$) are mono-disperse (with one particle fraction) and in 2D, one simulation (case #9.2D) is bi-disperse and in 2D, with two particle fractions. Finally, one intrusive particle-driven gravity current simulation (case #6.3D) is 3D. In the particle-driven cases, the salinity concentration trapped in the lock is replaced by a particle mixture. Three different Grashof numbers are investigated as well as two different interface thickness for the two-layer ambient fluid. These simulations have been designed to match the experimental set-up of Sutherland et al. (2004).

Table 1: Summary of density-driven and particle-driven simulations. β is the interface thickness between ambient fluids. The values in parenthesis for the case #9.2 are the proportion of fine and coarse particles. $Sc^{salt} = 10$ and $Sc^{part} = 20$ (for particle-driven). $Fr = 0.346$ (Fr - theoretical dimensionless front velocity), extracted from Sutherland et al. (2004).

Case	$\sqrt{Gr}$	β	u^s	mesh size (n_1, n_2, n_3)
#1.2D	1000	4π	0	1025×151
#2.2D	5000	4π	0	2049×257
#2.3D	5000	4π	0	$2049 \times 257 \times 193$
#3.2D	5000	20π	0	2049×257
#4.2D	10000	4π	0	4097×769
#5.2D	1000	4π	0.02	2049×201
#6.2D	5000	4π	0.02	3841×385
#6.3D	5000	4π	0.02	$3841 \times 385 \times 321$
#7.2D	5000	20π	0.02	3841×385
#8.2D	10000	4π	0.02	7681×769
#9.2D	10000	4π	0.02(40%) and 0.04(60%)	7681×769

The computational domain is discretised using an structured mesh with n_1, n_2, n_3 mesh nodes according to the Grashof number and settling velocity. As the Grashof number increases it is necessary increase the spatial resolution to capture all the turbulence scales. When the sedimentation is taking into account, stronger gradients are developed in the concentration field which also demands an increasing in spatial resolution. The spatial resolutions for these simulations have been chosen following a preliminary mesh refinement study to ensure that the discretisation errors are negligible for the quantities of interest presented in this manuscript. Note finally that the spatial resolutions used here are finer than the spatial resolutions used in our previous studies on gravity currents with the same flow solver, see Espath et al. (2014, 2015).

The following initial conditions seek to emulate the initial spatial density distribution presented in the experiments performed by Sutherland et al. (2004). In the density-driven cases, the salinity concentration is given by

$$
\begin{aligned}
&c = \frac{1}{2}; \quad b = \frac{1}{2} - \frac{1}{2}\tanh\left(x_2\sqrt{\frac{GrSc^{salt}}{\beta}}\right), \\
&\phi^{salt} = c + \frac{1}{2}(b-c)\tanh\left(x_1\sqrt{\frac{GrSc^{salt}}{\beta}}\right) + \frac{1}{2}(b-c),
\end{aligned}
\tag{17}
$$

where x_1 and x_2 are the origin $(0, 0)$, as see in figure 1. The coefficient β controls the initial interface thickness, that is, the greater β, the thicker the interface. Also, Gr and Sc influence the interface thickness.

In the particle-driven cases, the salinity concentration represents the density of the interstitial fluid as

$$
\begin{aligned}
&c = 0; \quad b = \frac{1}{2} - \frac{1}{2}\tanh\left(x_2\sqrt{\frac{GrSc^{salt}}{\beta}}\right), \\
&\phi^{salt} = c - \frac{1}{2}(b-c)\tanh\left(x_1\sqrt{\frac{GrSc^{salt}}{\beta}}\right) + \frac{1}{2}(b-c).
\end{aligned}
\tag{18}
$$

The particle concentration is trapped inside the lock and given by

$$
\begin{aligned}
&c = 1; \quad b = 0, \\
&\phi_a^{part} = c - \frac{1}{2}(b-c)\tanh\left(x_1\sqrt{\frac{GrSc_a^{part}}{\beta}}\right) + \frac{1}{2}(b-c), \\
&a = 1, \ldots, n_s^{part}.
\end{aligned}
\tag{19}
$$

For the initial condition, a weak perturbation is imposed on the velocity field at the lock-exchange interface to mimic the disturbances introduced in the flow when the mixture is released. The initial perturbation adds some initial kinetic energy not greater than 0.5% of the initial potential energy.

3.3. Flow Solver

The equations in the previous section are solved with a tailored version of the open-source high-order finite-difference solver `Incompact3d`, which is part of the `Xcompact3d` framework of flow solvers dedicated to the study of turbulent flows (Bartholomew et al., 2020). `Incompact3d` is based on compact sixth-order finite-difference schemes on a Cartesian mesh for the spatial differentiation and a third-order Adams–Bashforth scheme as the time integrator (other time integrators are available). The governing equations are solved with a fractional step method to treat the incompressibility constraint, which requires to solve an additional projection step, the Poisson equation. The Poisson equation is fully solved in spectral space using three-dimensional Fast Fourier Transforms(FFTs). More details about the code can be found in Laizet and Lamballais (2009). For the 3D simulations, the parallel version of `Incompact3d` based on a powerful 2D domain decomposition was used, see Laizet and Li (2011) for more details. The computational domain is split into a number of sub-domains (pencils) which are each assigned to an MPI-process. The derivatives and interpolations in the x-direction (y-direction, z-direction) are performed in X-pencils (Y-pencils, Z-pencils), respectively. The 3D FFTs required by the Poisson solver are also broken down as series of 1D FFTs computed in one direction at a time. Global transpositions to switch from one pencil to another are performed with the MPI command `MPI_ALLTOALL(V)`. `Incompact3d` can scale well with up to hundreds of thousands MPI-processes for simulations with several billion mesh nodes (Laizet and Li, 2011).

4. Results

4.1. Flow visualisations

When the lock gate is removed, The fluid in the lock is released and start accelerating in the two-layer ambient fluid, symmetrically in the present set-up. It then moves along the interface. A visual comparison between the experiment carried out in Sutherland et al. (2004) and the 2D simulation #2.2D is shown in figure 2. From top to bottom, in each figure, the experiment results, the salinity concentration, ϕ^{salt}, and the vorticity, ω are presented. Overall, there is a good agreement between the experiment and the present simulation, in particular with respect to the front evolution, which is almost identical. The main difference can be seen for the dimensions of the head of the intrusive current, with a smaller head in the experiment, suggesting that the current diffuses faster than in our simulation. This fact might be attributed to the smaller Schmidt number (due to computational constraints) in the simulation and to the uncertainties about the interface thickness between the two-layer ambient fluid. The difference in Schmidt number can also explain the highest level of turbulence activities in the tail for the present simulation while very little turbulence can be observed in the experiment. Such discrepancies for the turbulence activities at the tail of a gravity currents were also reported in Frantz et al. (2021).

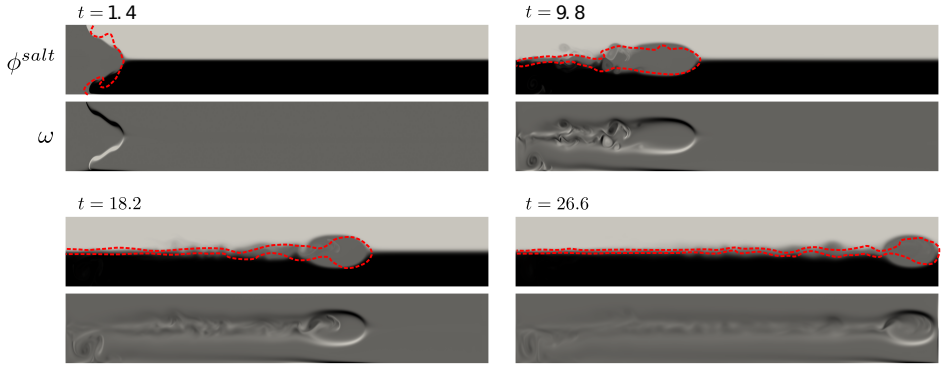

Figure 2: Visual comparison between the experiment Sutherland et al. (2004) and the numerical simulation (#2.2D). For the concentrations: black is 1, light gray is 0, and gray is 0.5. For the vorticity, normalized between 0 and 1: black is 1 and gray is 0. Dashed red lines represent the experimental result.

Figure 3 compares four two-dimensional density-driven simulations at time 11.6, when the intrusive current has nearly reached half of the computational domain in the streamwise direction. At the top of each subfigure the salinity concentration ϕ^{salt} is shown, whereas the vorticity ω, defined as $\omega = \mathrm{curl}\,\mathbf{v}$, is presented at the bottom. Except for the lowest Grashof number (case #1.2D), the current's head (the most prominent portion of the current with an ellipsoidal shape) shows a similar height and length. For case #1.2D, there is not a clear separation between the head and the tail. However, in the other cases the head and the tail are easily identified. Inspecting the salinity field it is possible to infer that the dimensions of the head are almost the same for all the cases. Behind the head, the tail of the current may propagate faster than the front, as previously reported in the literature for high Grashof numbers (Cheong et al., 2006).

It can also be seen that when the Grashof number is increased, the level of turbulence in the tail is more important. Virtually no turbulent structure can be observed for the lowest Grashof number (case #1.2D). No internal waves nor bores can be observed ahead of the head of the intrusive current, in agreement with previous simulations in a similar set-up (Khodkar et al., 2016). It can also be seen that there is no Kelvin-Helmoltz structures at the interface between the ambient and the head of the intrusive current (unlike the particle-driven cases). In addition, the case with the highest β (case #3.2D), that is, with thicker interface, shows a clear gap between the head and the tail. A greater salt diffusion in the case #1.2D can be observed in comparison to the other ones because the salt diffusion is inversely proportional to the square root of the Grashof number (see Eq. (13) and (14)).

Figure 4 presents a comparison of five two-dimensional particle-driven simulations at time 11.6. For the first four cases in this figure, from the top to the bottom of each subfigure, the particle concentration ϕ^{part},

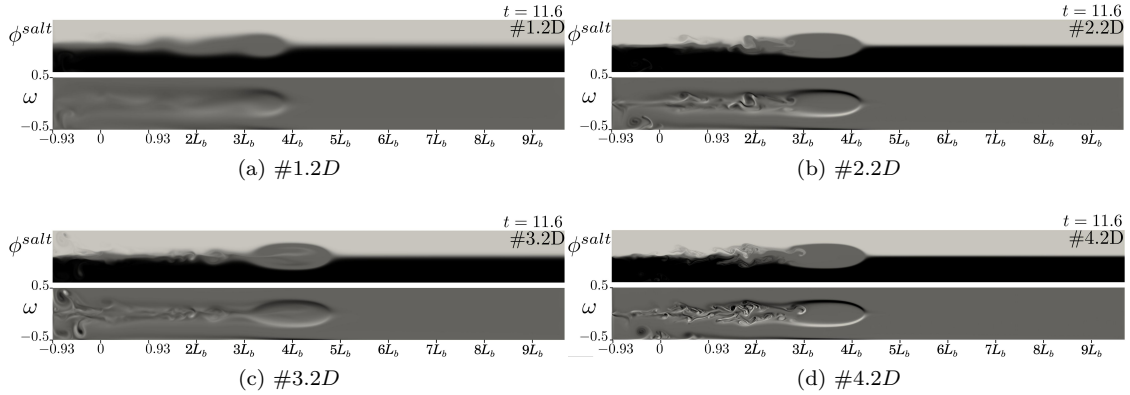

(a) #1.2D (b) #2.2D

(c) #3.2D (d) #4.2D

Figure 3: Plots of salinity (top) and vorticity (bottom) for density-driven cases (a) #1.2D, (b) #2.2D, (c) #3.2D and (d) #4.2D at $t = 11.6$. For the concentrations: black is 1, light gray is 0, and gray is 0.5. For the vorticity, normalized between 0 and 1: black is 1 and gray is 0.

salinity concentration ϕ^{salt}, and vorticity ω are presented. In the last subfigure, both particle concentrations, that is, ϕ_1^{part} (related to a settling velocity $u_1^s = 0.02$) and ϕ_2^{part} (related to a settling velocity $u_2^s = 0.04$) are plotted. Using as reference the particle concentration field, the current travels further in case #7.2D for which β is greater. Cases #5.2D and #9.2D, which are related to the lower Grashof number and bi-disperse case, respectively, show a slower development. The salinity fields show, except in the case #5.2D, a thicker head in comparison to the current head depicted by concentration field. In contrast to the density-driven cases, the head does not show a prominent shape, neither a clear separation between the head and the tail. Instead, the head present a wake form where fingering structures occur and interact with Kelvin–Helmoltz vortices. Thus, the process can be understood as a shear-stratified layer that forms fingers. Looking at the tail, in the vorticity subfigures (see for instance Figure 4d and 4e), a nonstandard finger formation can be observed. It is nonstandard in the sense that many fingers are not symmetric at all. The lack of symmetry is rendered by the Kelvin–Helmholtz vortices, that is, fingers and Kelvin–Helmholtz vortices are developed together. In contrast to hyperpycnal flows (Espath et al., 2014, 2015; Francisco et al., 2018), there is a clear difference in the head's shape between density- and particle-driven cases. Here, the head has an almost flat surface at the top and a wavy shape at the bottom differing significantly from an ellipsoidal symmetric shape. In the bi-disperse case (#9.2D), the heavier particles are slowing down the evolution of the current with a faster deposition process. Another interesting feature is that the finger formation occurs at different heights, where two layers of fingers are settling. This is a clear suggestion that the finger formation by different particle weight are formed independently.

Figure 5 shows the comparison between the two- and three-dimensional for the particle-driven case at times 10.0, 12.0, 14.0, and 16.0 for the particle concentration. Although two-dimensional simulations can appropriately model the main features of a three-dimensional intrusive gravity current, there are particularities and, mainly, instabilities that only occurs in three-dimensional simulations. For instance, comparing 5a-5d, the formation of one layer of fingers in the tail of the current can be observed for the 2D simulation, whereas in the three-dimensional case, there are at least three layers of fingers that occur at different heights. The good agreement, regarding the front features, namely the front velocity, suggests that the 3D instabilities do not affect the evolution of the intrusive current. It can also be observed that the mixing at the start of the tail is more efficient in 3D than in 2D (for the 2D, large scale coherent structures can be observed while for the 3D case the tail is much more diffuse than for the 2D case).

Figure 6 shows the three-dimensional evolution of the density-driven current (#2.3D) at times 4.0, 8.0, 12.0, and 16.0, with two isosurfaces of salinity concentration for $\phi = 0.49$ and $\phi = 0.51$ and the isosurface of Q-criterion, $Q = 1$. Q is defined as $Q = \frac{1}{2}(\Omega_{ij}\Omega_{ij} - S_{ij}S_{ij})$, where Ω_{ij} is the antisymmetric component of grad u, and S_{ij} the symmetric one. In this figure, it can be seen that the head of the current is predominantly two-dimensional, even though a small perturbation in the velocity field near the gate was introduced in the

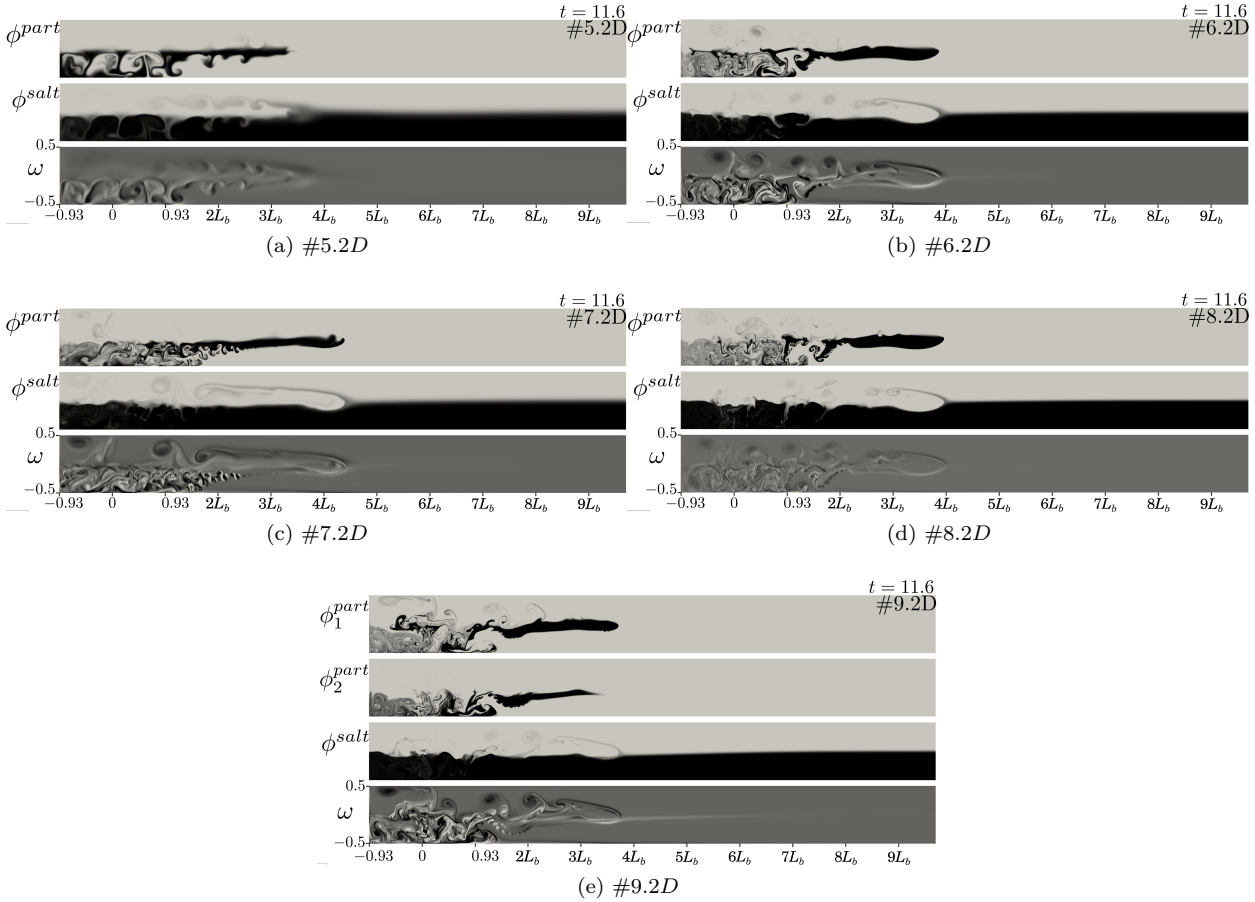

(a) #5.2D (b) #6.2D

(c) #7.2D (d) #8.2D

(e) #9.2D

Figure 4: Comparison of particle-driven cases (a) #5.2D, (b) #6.2D, (c) #7.2D, (d) #8.2D and (e) #9.2D at $t = 11.6$. In each figure, from top to bottom are plotted the particle concentration, the salinity and the vorticity fields. For the concentrations: black is 1 and light gray is 0. For the vorticity, normalized between 0 and 1: black is 1 and gray is 0.

initial condition. This suggests that this perturbation was quickly damped and nearly annihilated, very likely because of the strong acceleration of the intrusive current at the start of the simulations. Conversely, three-dimensional structures are observed at the tail and at the sub-current intruding behind the head, see also Figure 6b. This sub-current is slightly faster than the main current, and it does not seem to affect the main features of the current. At time $t = 16.0$ the head is still two-dimensional, whereas the tail and the sub-current exhibit three-dimensional turbulent structures. Besides the sub-current, the overall shape is quite symmetric with respect the horizontal plane, as expected and consistently with previous results (Khodkar et al., 2016).

Figures 7 show the three-dimensional evolution of the particle-driven current (#6.3D) at times 4.0, 8.0, 12.0, and 16.0, with an isosurface of particle concentration $\phi^{part} = 0.25$, the salinity concentration $\phi^{salt} = 0.5$, and the isosurface of Q-criterion $Q = 1$. A clear effect caused by the settling velocity is the lack of symmetry with respect to the horizontal plane, even at the very early stages of the simulation. For time $t < 4.0$, looking at the Q-isosurface, the head has a symmetric and two-dimensional structure. As time goes by, the structure defining the top of the head gradually disappears, whereas the bottom one remains two-dimensional. At time $t = 12.0$, the two-dimensional structure at the top of the head is gone, giving place to three-dimensional structures with horseshoe or U shape.

To better analyse the three-dimensional structures that appear right after the tail of the current, figure 8 presents both concentration and Q-criterion fields for the case #6.3D. There is an interaction between the

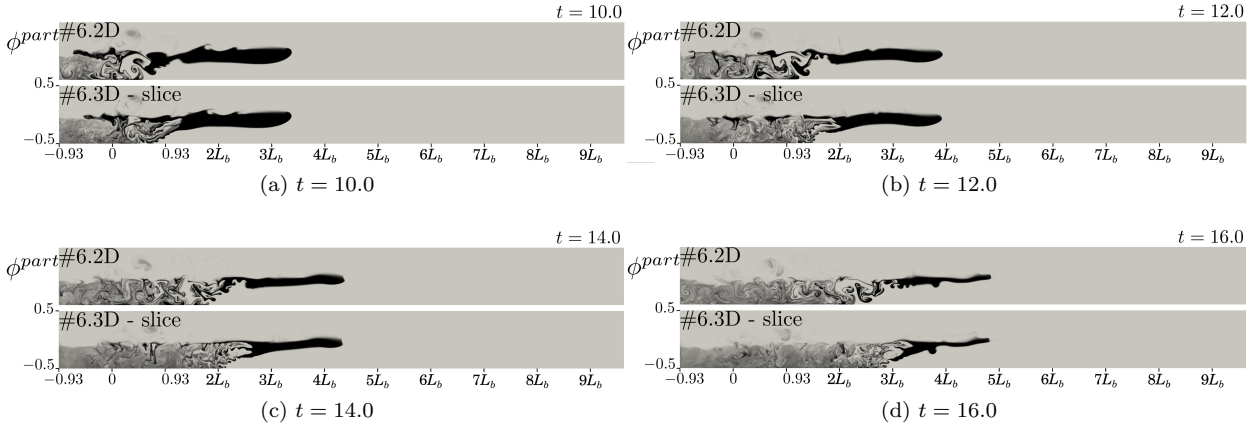

(a) $t = 10.0$ (b) $t = 12.0$

(c) $t = 14.0$ (d) $t = 16.0$

Figure 5: Comparison between two- and three-dimensional simulation in particle-driven case, $\#6.2D$ vs $\#6.3D$, for (a) $t = 10.0$, (b) $t = 12.0$, (c) $t = 14.0$ and (d) $t = 16.0$. The three-dimensional snapshots were taken in a plane located at $x_2 = 0$. Black is 1 and light gray is 0.

Kelvin–Helmholtz vortices, triggered by the stratification on both velocity and density as well as the fingering instability, triggered by the particle-salinity stratification, as mentioned before. Fingers are usually developed with a mushroom-shaped structure when the fluid only shows stratification in the density field. Due to velocity stratification, the development of Kelvin–Helmholtz instabilities misshape the finger structures, changing the usual mushroom type of structure (Farenzena and Silvestrini, 2017; Burns and Meiburg, 2015). At time 5.8, stretched fingers align with the streamwise direction can be observed. Then, at times 10.0 and 15.2, a set of squeezed fingers is observed with a ring-shaped structure. It should also be noted that the fingers are getting bigger and bigger when the simulation is advanced in time. Further investigations are needed to investigate the potential correlation between the number of fingers in the spanwise direction, the Grashof number and the settling velocity.

4.2. Front Evolution

In the density driven intrusive currents the front evolution is linear. Also, as noticed by Sutherland et al. (2004), the front evolution is not affected by the subcurrent intruding into the head of the main current. Our results, $(\#2.2D, \#2.3D, \#4.2D)$ with $Fr \approx 0.33$, predict the theoretical $Fr = 0.346$ and experimental results (Sutherland et al., 2004) to a great extent. The small discrepancy, which is less than 5%, may be attributed to the fact that our Grashof number is smaller (due to computational constraints) than the the experimental one. When the interface thickness is increased, $\#3.2D$, so is the front velocity. Conversely, the front velocity is reduced when the Grashof number is decreased, $\#1.2D$. In Table 2, we present the front velocity ($v_F = Fr$) of all density driven cases. The two- and three-dimensional simulations present the same front velocity.

Table 2: Front velocity for density driven cases.

Case	$v_f(Fr)$
#1.2D	0.293
#2.2D	0.332
#2.3D	0.332
#3.2D	0.384
#4.2D	0.338

Figure 9 depicts the front evolution for the particle-driven cases. As observed in the density-driven cases, also shows a good agreement between the two- and three-dimensional simulations. As for the dependency

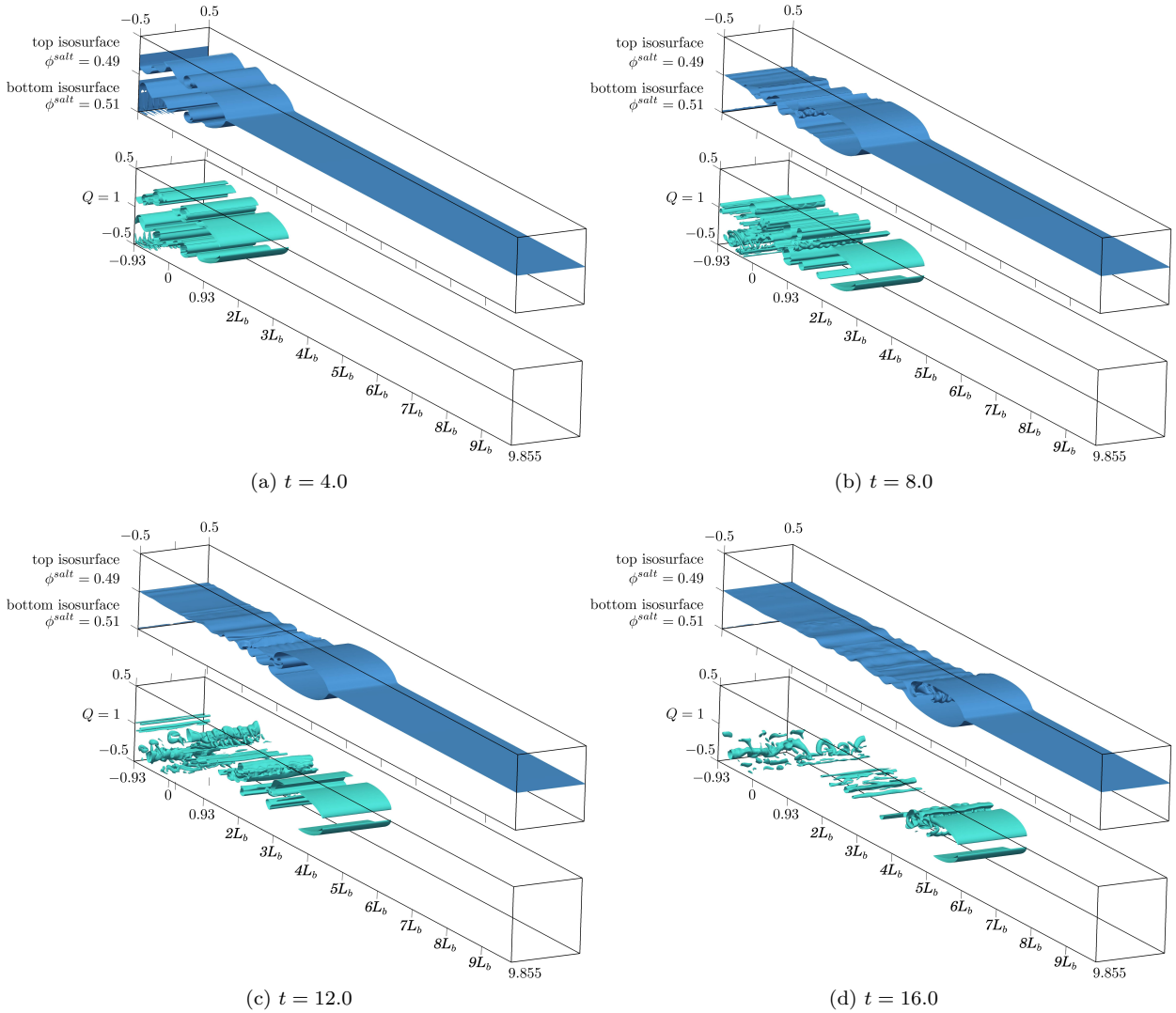

(a) $t = 4.0$ (b) $t = 8.0$

(c) $t = 12.0$ (d) $t = 16.0$

Figure 6: (Color online) Isosurfaces of saline concentration (top) and Q-criterion (bottom) for density-driven case #2.3D at (a) $t = 4.0$, (b) $t = 8.0$, (c) $t = 12.0$ and (d) $t = 16.0$. Concentration is taken for $\phi^{salt} = 0.49$ and 0.51 and Q-criterion is taken for $Q = 1$.

on the Grashof number Gr, at early stages the front velocity is roughly the same for all Gr, with a value of $v_f \approx 0.342$. The velocity starts decreasing right after the beginning of the sedimentation process. Higher Grashof numbers Gr, imply in low diffusion. Thus, the deceleration is higher with the decrease of Gr. The front evolution is nearly linear at early stages since no suspended mass is lost due to deposition. Figure 9b shows the influence of the interface thickness. Increasing the initial interface thickness, from $\beta = 4\pi$ to $\beta = 20\pi$, the front velocity changes at early stages, from 0.309 (#6.2D) to 0.351 (#7.2D). After $t \approx 12.5$ the velocities are almost the same. Also, Figure 9c shows the front velocity for the bi-disperse case #9.2D compared against its mono-disperse version #8.2D. In the bi-disperse case, we present two curves, one for each particle fraction. At the early stages of the flow, from $t = 0$ up to $t \approx 5$, both fronts present the same linear development, showing that the initial behavior of the current is mainly ruled by de Grashof number, independently of its granulometry. After $t \approx 5$, the both fronts start slowing down due to the presence of heavier particles, referred as particle 2 ($u_s = 0.04$, 60% in concentration). Owing to heavier particles in the

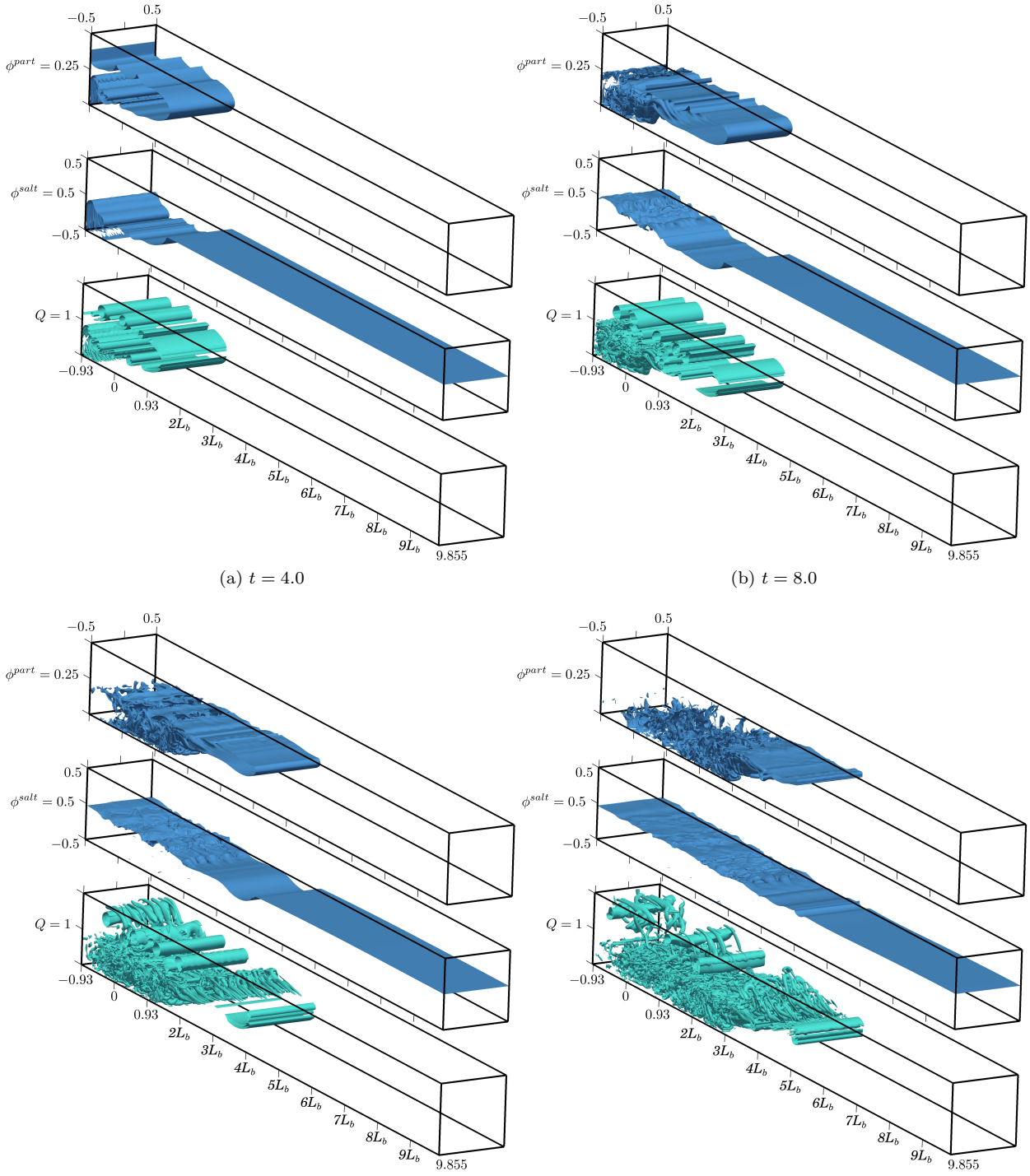

(a) $t = 4.0$ (b) $t = 8.0$

(c) $t = 12.0$ (d) $t = 16.0$

Figure 7: (Color online) Flow evolution of particle-driven case #6.3D at (a) $t = 4.0$, (b) $t = 8.0$, (c) $t = 12.0$ and (d) $t = 16.0$. Isosurfaces taken for $\phi^{part} = 0.25$, $\phi^{salt} = 0.5$ and $Q = 1$.

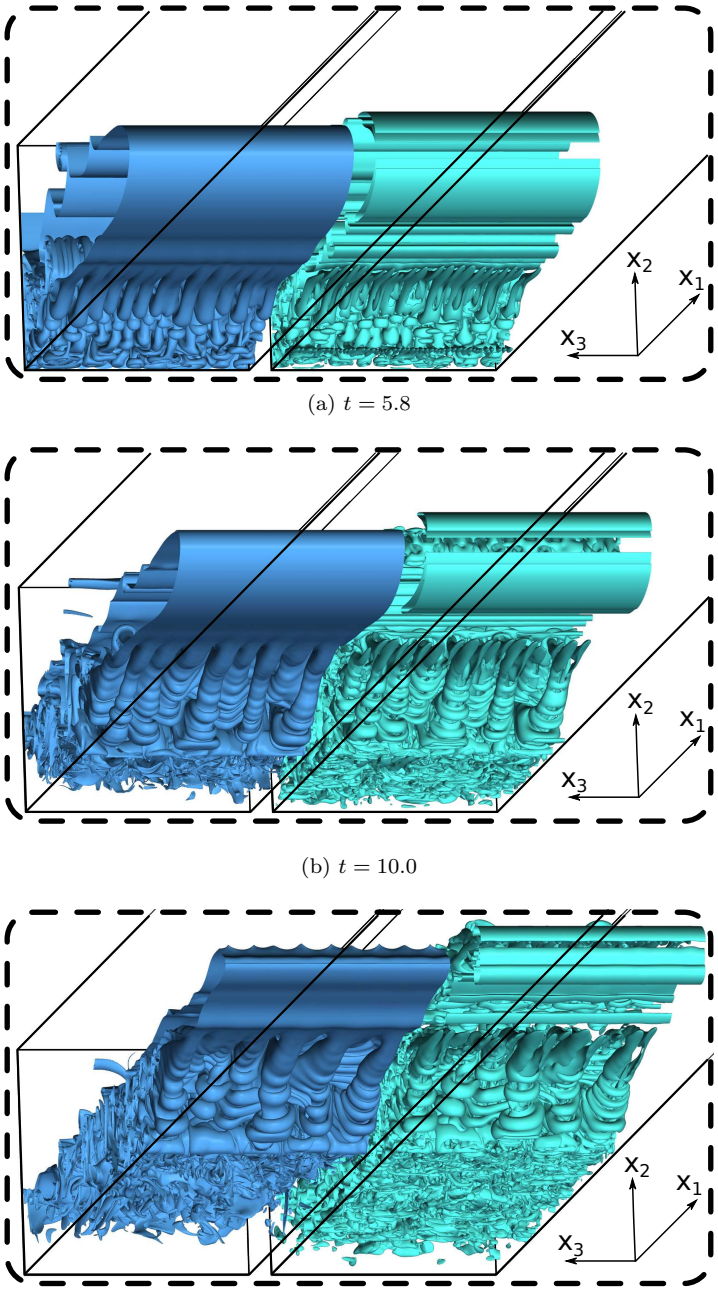

(a) $t = 5.8$

(b) $t = 10.0$

(c) $t = 15.2$

Figure 8: (Color online) Detail of concentration (left) and Q-criterion (right) fields for the particle-driven case #6.3D at (a) $t = 5.8$, (b) $t = 10.0$ and (c) $t = 15.2$. Bottom view.

mixture, these are sedimented faster than lighter ones so that the current inertia decreases due to mass loss through deposition.

The curve referred as particle 1 ($u_s = 0.02$, 40% in concentration) evolves further due to a lower settling velocity. However, heavier particles' presence decelerates the overall velocity of the current, which means that smaller and lighter particles are affected by the heavier ones in an indirect manner since no cross diffusion is considered.

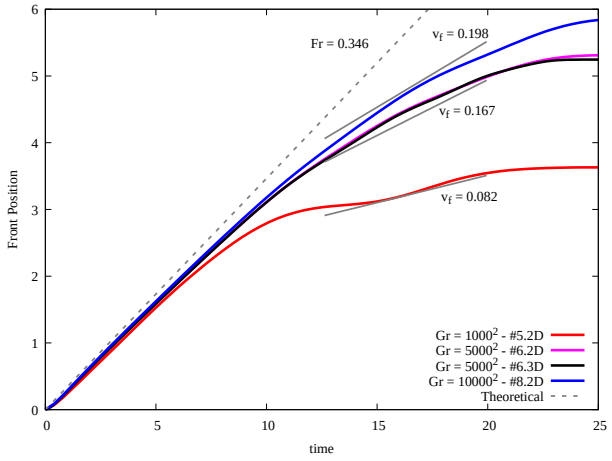

(a) Cases #5.2D, #6.2D, #6.3D and #8.2D

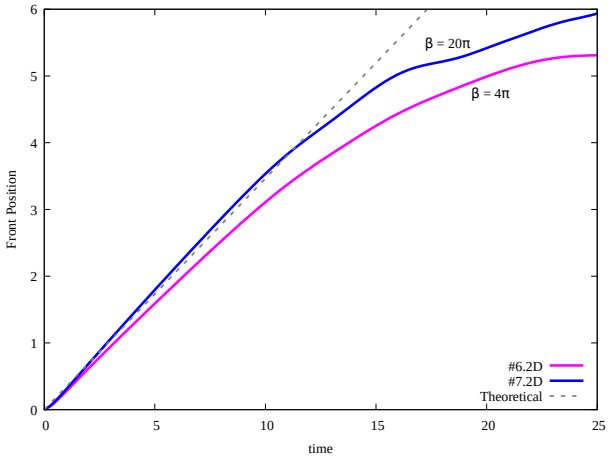

(b) Cases #6.2D and #7.2D

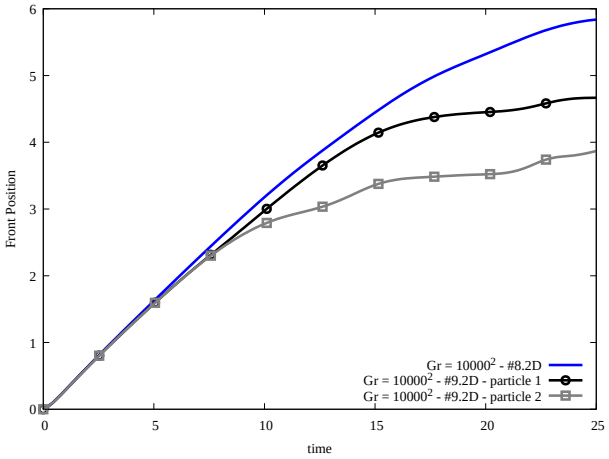

(c) Cases #8.2D and #9.2D

Figure 9: (Color online) Front evolution in particle-driven cases: 9a) Grashof influences 9b) Thickness in the initial condition influences 9c) mono- and bi-disperse cases. Dashed line is the theoretical result of Sutherland et al. (2004) is also plotted.

4.3. Energy budget

The energy budget allows us to understand and measure the energy transfer as well as the dissipation mechanisms. Here, following Espath et al. (2016), we generalize the derivation in Espath et al. (2014, 2015). We consider the energy exchanges across the boundaries and express the dissipations in terms of the Cauchy stress tensor and the mass flux, which allows us to interpret the energy losses in a general context, such as in the presence of a complex topography.

Consider the material derivative of each energy involved in the problem, that is, $\dot{e}_\jmath$ where $\jmath = \{k, p\}$, where e_k represents kinetic energy, e_p^{salt} salt-water potential energy, and $e_{p,a}^{part}$ the a-th particle-water potential energy. Integrating these material derivatives over the domain results in the total derivative $\mathrm{d}(\cdot)/\mathrm{d}t$ of each energy. In what follows, we use an Eulerian description, that is, we consider the equations formulated for a given control volume Ω and boundary Γ, as

$$\frac{\mathrm{d}E_\jmath}{\mathrm{d}t} = S_\jmath + Q_\jmath = \int_\Gamma \epsilon_\jmath^{io}\,\mathrm{d}\Gamma + \int_\Omega \epsilon_\jmath\,\mathrm{d}\Omega, \tag{20}$$

where, as before, $\jmath = \{k, p\}$ denotes the energy type. The term $Q_\jmath$ incorporates the sources and sinks of the energy $E_\jmath$ in the control volume, and $S_\jmath$ is the total diffusive flux of energy across the boundary of the control volume. Integrating over time the quantity $S_\jmath + Q_\jmath$, we obtain the quantities that describe energy dissipation. Here, we denote the extensive (intensive) quantities by uppercase (lowercase) letters, such as, $E_{(\cdot)}$ ($e_{(\cdot)}$) for the extensive (intensive) energies and $\mathcal{E}_{(\cdot)}$ ($\epsilon_{(\cdot)}$) for the extensive (intensive) dissipation.

The energies of the system, namely, kinetic E_k and potential energies of salt-water E_p^{salt} and a particle solutions $E_{p,a}^{part}$ are defined as follows.

$$\begin{aligned} E_k &= \int_\Omega e_k \,\mathrm{d}\Omega = \int_\Omega \frac{1}{2}\mathbf{v}\cdot\mathbf{v}\,\mathrm{d}\Omega, \\ E_p^{salt} &= \int_\Omega e_p^{salt}\,\mathrm{d}\Omega = \int_\Omega \frac{1}{2}x_2\alpha_0\phi^{salt}\,\mathrm{d}\Omega, \\ \sum_{a=1}^{n_s} E_{p,a}^{part} &= \sum_{a=1}^{n_s}\int_\Omega e_{p,a}^{part}\,\mathrm{d}\Omega = \sum_{a=1}^{n_s}\int_\Omega \frac{1}{2}x_2\alpha_a\phi_a^{part}\,\mathrm{d}\Omega. \end{aligned} \tag{21}$$

From the governing equations, we obtain the energy dissipation related to each energy as

$$\begin{aligned} Q_k = \int_\Omega \epsilon_k\,\mathrm{d}\Omega &= \int_\Omega \left(-\mathbf{D}:\mathbf{T} - b_\rho v_2\right)\,\mathrm{d}\Omega, \\ &= \int_\Omega \left(-\frac{2}{\sqrt{Gr}}\mathbf{D}:\mathbf{D} - b_\rho v_2\right)\,\mathrm{d}\Omega, \end{aligned} \tag{22a}$$

$$\begin{aligned} \sum_{a=1}^{n_s} Q_{p,a}^{part} = \sum_{a=1}^{n_s}\int_\Omega \epsilon_{p,a}^{part}\,\mathrm{d}\Omega &= \sum_{a=1}^{n_s}\int_\Omega \left(\alpha_a\,\mathbf{j}_a^{part}\cdot\mathbf{e}_2 + \alpha_a\phi_a^{part}v_2\right)\,\mathrm{d}\Omega, \\ &= \sum_{a=1}^{n_s}\int_\Omega \left[\left(-\frac{\alpha_a}{\sqrt{Gr(Sc_a^{part})^2}}\,\mathrm{grad}\,\phi_a^{part} + \alpha_a\phi_a^{part}\mathbf{v}_a^s\right)\cdot\mathbf{e}_2 + \alpha_a\phi_a^{part}v_2\right]\,\mathrm{d}\Omega, \end{aligned} \tag{22b}$$

$$\begin{aligned} Q_p^{salt} = \int_\Omega \epsilon_p^{salt}\,\mathrm{d}\Omega &= \int_\Omega \left(\alpha_0\,\mathbf{j}^{salt}\cdot\mathbf{e}_2 + \alpha_0\phi^{salt}v_2\right)\,\mathrm{d}\Omega, \\ &= \int_\Omega \left[-\frac{\alpha_0}{\sqrt{Gr(Sc^{salt})^2}}\mathrm{grad}\,\phi^{salt}\cdot\mathbf{e}_2 + \alpha_0\phi^{salt}v_2\right]\,\mathrm{d}\Omega. \end{aligned} \tag{22c}$$

The last term of each dissipation cancels out in the total sum.

Next, also from the governing equations, the input/output energies across the boundaries are

$$S_k = \int_\Gamma \epsilon_k^{io}\,\mathrm{d}\Gamma = \int_\Gamma \mathbf{v}\cdot\mathbf{T}\cdot\mathbf{n}\,\mathrm{d}\Gamma,$$
$$= \int_\Gamma \mathbf{v}\cdot\left[-p\mathbf{I} + \frac{2}{\sqrt{Gr}}\mathbf{D}\right]\cdot\mathbf{n}\,\mathrm{d}\Gamma, \tag{23a}$$

$$S_p^{part} = \int_\Gamma (\epsilon_{p,a}^{part})^{io}\,\mathrm{d}\Gamma = \sum_{a=1}^{n_s}\int_\Gamma -x_2\alpha_a\,\mathbf{j}_a^{part}\cdot\mathbf{n}\,\mathrm{d}\Gamma,$$
$$= \sum_{a=1}^{n_s}\int_\Gamma -x_2\left(-\frac{\alpha_a}{\sqrt{Gr(Sc_a^{part})^2}}\,\mathrm{grad}\,\phi_a^{part} + \alpha_a\phi_a^{part}\mathbf{v}_a^s\right)\cdot\mathbf{n}\,\mathrm{d}\Gamma, \tag{23b}$$

$$S_p^{salt} = \int_\Gamma (\epsilon_p^{salt})^{io}\,\mathrm{d}\Gamma = \int_\Gamma -x_2\alpha_0\,\mathbf{j}^{salt}\cdot\mathbf{n}\,\mathrm{d}\Gamma,$$
$$= \int_\Gamma -x_2\left(-\frac{\alpha_0}{\sqrt{Gr(Sc^{salt})^2}}\,\mathrm{grad}\,\phi^{salt}\right)\cdot\mathbf{n}\,\mathrm{d}\Gamma. \tag{23c}$$

Here, we address the energy budget of the system. Integrating the source and sink terms along with the fluxes over time leads to the total energy exchange terms, where one can define the volumetric terms as

$$\mathcal{E}_\jmath = \int_t Q_\jmath\,\mathrm{d}t = \int_t\int_\Omega \epsilon_\jmath\,\mathrm{d}\Omega\mathrm{d}t, \qquad \jmath = \{k,p\}, \tag{24}$$

and the input/output of energy diffused across the boundaries is

$$\mathcal{E}_\jmath^{io}\Big|_{diff} = \int_t S_\jmath\,\mathrm{d}t = \int_t\int_\Gamma \epsilon_\jmath^{io}\Big|_{diff}\mathrm{d}\Gamma\mathrm{d}t, \qquad \jmath = \{k,p\}. \tag{25}$$

If there exists a momentum flux across the boundaries, the energy must be advected according to

$$\mathcal{E}_\jmath^{io}\Big|_{adv} = -\int_t\int_\Gamma e_\jmath\,\mathbf{v}\cdot\mathbf{n}\,\mathrm{d}\Gamma\mathrm{d}t, \qquad \jmath = \{k,p\}, \tag{26}$$

and the sum of $\mathcal{E}_\jmath^{io}\Big|_{diff} + \mathcal{E}_\jmath^{io}\Big|_{adv}$ yields the total input/output of energy across the boundaries.

Finally, the energy budget is

$$E_k + E_p - (\mathcal{E}_k + \mathcal{E}_p + \mathcal{E}_k^{io} + \mathcal{E}_p^{io}) = C, \tag{27}$$

for an arbitrary constant C. We analyze the energy exchange over the whole domain and use no-flux boundary conditions for all fields in the numerical examples discussed in the following. Since the flux of particles through the bottom occurs at $x_2 = 0$ there is no potential energy loss. Under such setup, the energy budget equation reads

$$\sum_{\jmath=\{k,p\}} (E_\jmath - \mathcal{E}_\jmath)(t) = E_k + E_p - (\mathcal{E}_k + \mathcal{E}_p) = C. \tag{28}$$

As before, we relate $E_\jmath$ and $\mathcal{E}_\jmath$, $\jmath = \{k,p\}$, to extensive energies and their energy exchanges, whereas we associate $e_\jmath$ and $\epsilon_\jmath$ to intensive energies and their energy exchanges, respectively.

The energy dissipations are, in general, related to the momentum and species fluxes, as follows:

- ϵ_k is related to the shear stress or to the turbulent dissipation at the macroscipic scales (momentum diffusion);
- $\epsilon_{p,i}^{part}$ is originated by the particle concentration flux in the gravitational direction;

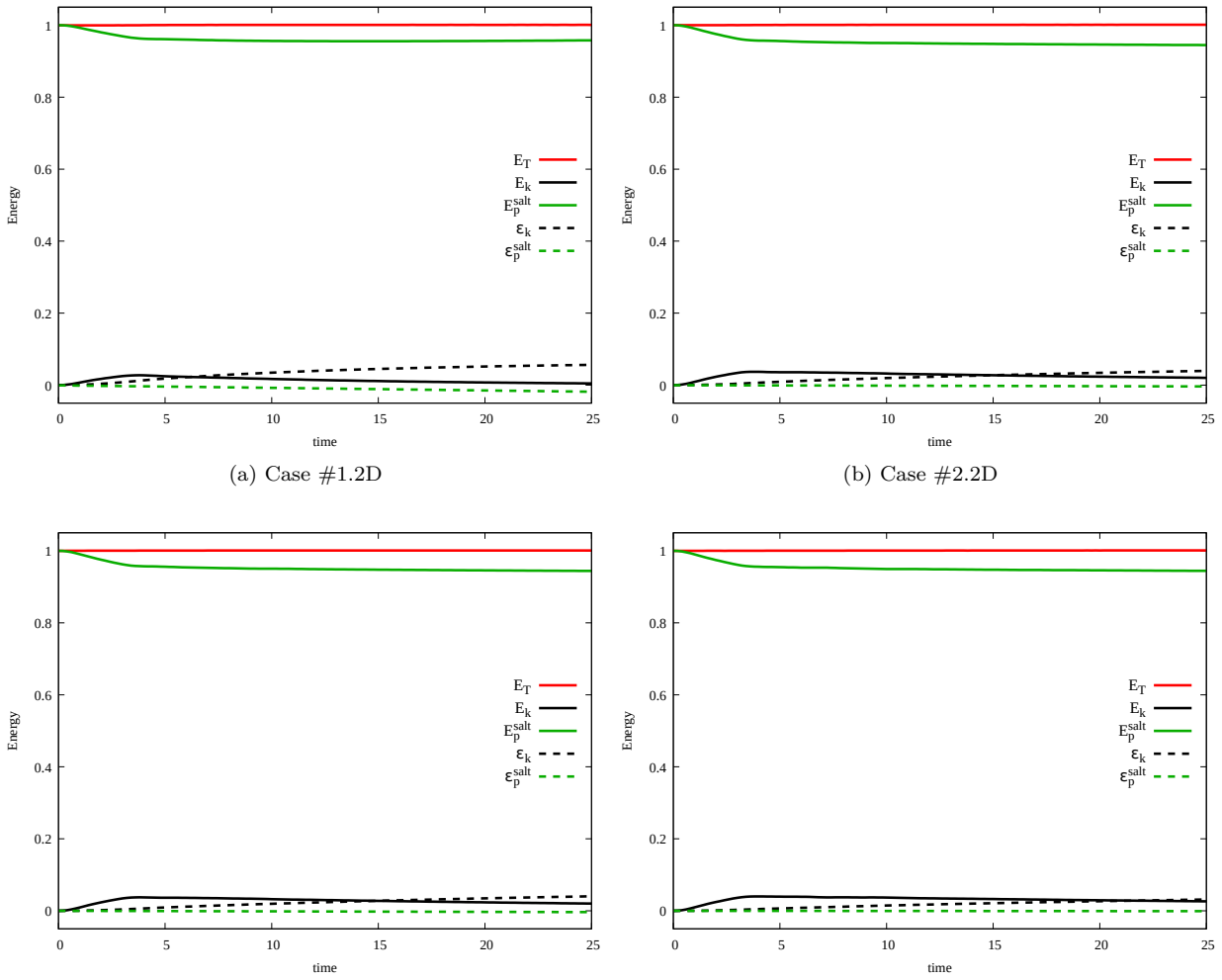

(a) Case #1.2D (b) Case #2.2D

(c) Case #2.3D (d) Case #4.2D

Figure 10: (Color online) Energy evolution in density-driven cases (a) #1.2D, (b) #2.2D, (c) #2.3D and (d) #4.2D.

- ϵ_p^{salt} is caused by the salinity flux in the gravitational direction.

While, the input/output energies are related to the energies that enter or leave the domain across its boundaries, that is,

- $\mathbf{v} \cdot \mathbf{n} < 0$ on Γ: input kinetic energy;
- $\mathbf{v} \cdot \mathbf{n} > 0$ on Γ: output kinetic energy;
- $(\mathbf{j}_a^{part}, \mathbf{j}^{salt}) \cdot \mathbf{n} < 0$ on Γ: input potential energy;
- $(\mathbf{j}_a^{part}, \mathbf{j}^{salt}) \cdot \mathbf{n} > 0$ on Γ: output potential energy.

In Figures 10 and 11, we respectively present the energy budget of the flows for the density- and particle-driven cases. Solid lines represent energies, whereas dashed lines represent their dissipations. The red line shows the energy conservation, showing that our direct numerical approach conserves energy. The green solid (dashed) line represents the potential energy (dissipation) due to salinity concentration, whereas the

blue solid (dashed) line represents the potential energy (dissipation) due to particle concentration. In the bi-disperse case, the energy and dissipation related to the second particle concentration are in magenta. Last, the blue solid (dashed) line represent the kinetic energy (dissipation).

In the density-driven simulations, the kinetic (potential) energy increases (decreases) up to $t \approx 3$. During this initial phase, the main energy exchange mechanism occurs between the kinetic and potential energy (see, for instance Figure 10). After, the evolution of these energies decay at a very slow rate due to dissipation. For the lowest Grashof number, the potential energy does not decay as much as for higher Grashof numbers. Likewise, the kinetic energy for the lowest Grashof number has also the lowest peak. On the other hand, the highest peak in the kinetic energy occurs for the highest Grashof number. This implies that for higher Grashof numbers a greater amount of energy is converted to kinetic energy.

In the particle-driven simulations there is a similar energy exchange behavior between the potential energy due to the salinity and kinetic energy when compared with the density-driven cases (see, for instance Figure 11). However, in these simulations, the potential energy due to the particle-fluid mixture plays an important role. Here, the main difference is that there is an additional energy exchange between potential energy due to particle-fluid mixture and kinetic energy. Moreover, owing to the settling of particles, which in turn damp the turbulence, the kinetic energy decays much faster. In contrast to the potential energy due to the salinity, the potential energy due to the particles continuously decay and eventually disappears. Last, our discretization conserves the total energy within an acceptable numerical error as shown in these figures as well.

Dissipation in intrusive gravity currents is significantly smaller than the dissipation observed in turbidity currents (compare, for instance Necker et al. (2005); Espath et al. (2014, 2015)). Turbidity currents present an enormous dissipation of the kinetic energy due to boundary layer effects. Since in intrusive currents these effects are almost nonexistent, the dissipation is much less relevant. Indeed, the boundary effects only occur at early stages, when the current is still in contact with the bottom wall. For this reason, the dissipation of the kinetic energy (see Figures 10 and 11) is only noticeable at the very beginning, remaining almost constant when all the current is inside the interstitial fluid.

4.4. Suspended material and sedimentation rate

Other relevant features for which we track their temporal evolution in this kind of flow are the suspended mass of the particle mixture and sedimentation rate. We compute the total amount of suspended material by integrating the concentration of each particle fraction over the entire domain as follows.

$$m_p(t) = \sum_{a=1}^{n_s} \int_\Omega \phi_a^{part}(\mathbf{x})\, \mathrm{d}\Omega, \tag{29}$$

and the advective sedimentation rate is

$$\dot{m}_s(t) = \sum_{a=1}^{n_s} \frac{1}{L_{1b} L_{3b}} \int_0^t u_a^s \phi_{a_w}^{part}(x_1, x_3, t)\, \mathrm{d}t, \tag{30}$$

where $\phi_{a_w}^{part}$ is the a-th particle concentration at the bottom wall, that is, $x_2 = -L_{2b}/2$.

Figure 12 presents the temporal evolution of the suspended mass. In Figure 12a, we evaluate the effect of the Grashof number while in Figure 12b, we study the presence of more than one particle fraction changes the overall behavior of the suspended mass. Differently from the front position, suspended mass does not show a strong dependency on the Grashof number. The noticeable different occurs only for the smallest Grashof number. Figure 12a shows that up to $t \approx 3$ the suspended mass for all mono-disperse cases is almost the same. After that time, significant difference between curves for $Gr = 1000^2$ and $Gr = 5000^2$ are seen, but the same is not observed between $Gr = 5000^2$ (both 6.2D 6.3D) and $Gr = 10000^2$ (8.2D). The current is weakly affected by the three-dimensional configuration, showing that the turbulence generated by the spanwise dimension's inclusion is not important to keep the mass in suspension. The assessment of the bi-disperse case (Fig. 12b) shows a fast decreasing of the suspended mass when heavier particles are added in the mixture compared to the mono-disperse one, considering the same Grashof number. Interestingly, in

the bi-disperse case, each particle type shows a distinct behavior. The mass of the lighter particles decreases almost constantly reaching, at the end of the simulation, a little less than 50% of its initial mass. On the other hand, the heavier particles smoothly decrease from $t = 0$ up to $t \approx 5$. From $t \approx 5$ up to $t \approx 22$ they sharply decrease by $\approx 80\%$ in its suspended mass. After $t \approx 22$ up to the end, the mass decrease becomes smooth again, being almost zero, which means that, at time 25.0, almost all suspended mass is due to the presence of lighter particles. Comparing the overall behavior between mono and bi-disperse currents, we observe that for a mixture including 60% of heavier particles and 40% of lighter ones, its final suspended mass is almost 50% less than a current with only lighter particles.

Figure 13 shows the sedimentation rates. Figure 13a presents all mono-disperse cases while Figure 13b shows the comparison between mono- versus bi-disperse cases. In all cases the sedimentation rate starts with a strong decay, except for the cases $\#5.2D$ and $\#9.2D$, up to the point where the current flows completely as an intrusive gravity current. After this point, no boundary layer effects, arising from the particle-mixture contact with no-slip walls, affect the current. Between $t \approx 3$ and $t \approx 7$ (depending upon the case) the sedimentation rate for the cases $\#6.2D$, $\#6.3D$ and $\#8.2D$ falls to zero, as observed in Figure 12, where the suspended mass remains constant during this time interval. As for the three-dimensional case $\#6.3D$, this period of zero sedimentation rate is abbreviated specially when compared to its corresponding bi-dimensional case. Broadly speaking, the sedimentation rate grows proportional to $t^{1.05}$ after $t \approx 10.0$. Then, after $t \approx 20.0$, for the lowest Grashof number, case $\#5.2D$, where there is not enough suspended mass to keep its sedimentation rate constant, we observe a slight decay in the rate. This is not the case of the highest Grashof number, case #8.2D, where the sedimentation rate is still constant up to $t = 25$, the end of the simulation. For those cases where the sedimentation rate decreases after $t \approx 20$, they seem to follow a power law of $t^{-1.59}$.

Taking the cases $Gr = 5000^2$ (both 6.2D 6.3D) and $Gr = 10000^2$ (8.2D), three clear stages are observed. In the first stage $t < 3$, the dilute suspension of particles is still in contact with the bottom wall, there is a nearly constant sedimentation rate. Thus, the suspended mass decreases linearly. In the second stage $3 < t < 7$, the particle-driven intrusive current is not in contact with the bottom wall and there is no sedimentation at all. Consequently, the suspended mass is constant. In the third stage, finger structures from the dilute particle suspension start to deposit at a fairly constant rate. Thus, the suspended mass decreases at a constant rate. These three stages are less evident for the smallest Grashof number and the bi-disperse cases, where the second stage is not present.

4.5. Deposit Map

Figure 14 depicts two- and three-dimensional deposit profiles; Figure 14a (left) shows all the mono-disperse two-dimensional cases; Figure 14b (right) compares the mono- and bi-disperse cases. Figure 14a shows that as the Grashof number grows, the deposit profile becomes thinner, which relates to the fact that the current travels further for higher Grashof numbers, spreading the particles over a larger area. A higher amount of suspended material is deposited at early stages, which is more evident when the Grashof number decreases. Concerning the three-dimensional simulation, the deposit profile is smoother than in its two-dimensional version; Espath et al. (2014) reported similar behavior.

Figure 15 shows the three-dimensional deposit map at times 7.0, 11.0, 15.0, 19.0, and 24.0. In contrast to the results of Espath et al. (2015), where the lobe-and-cleft structures leave a strong and clear fingerprint pattern on the deposit map, here we cannot identify a single pattern; however, the deposit at the head of the deposition map in Figures 15b-15e) has a length (roughly $\approx h/2$) in the spanwise direction and the wave-length (roughly $\approx h/5$ to $h/6$) in the streamwise direction. Conversely, the sediments coming after the head introduce and additional pattern with this extra deposit layer. More research needs to be done to fully understand the whole pattern, which is more intricate than those found in turbidity currents.

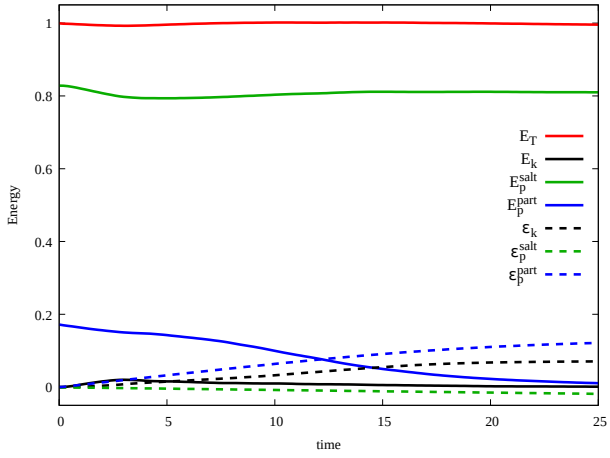

(a) Case #5.2D

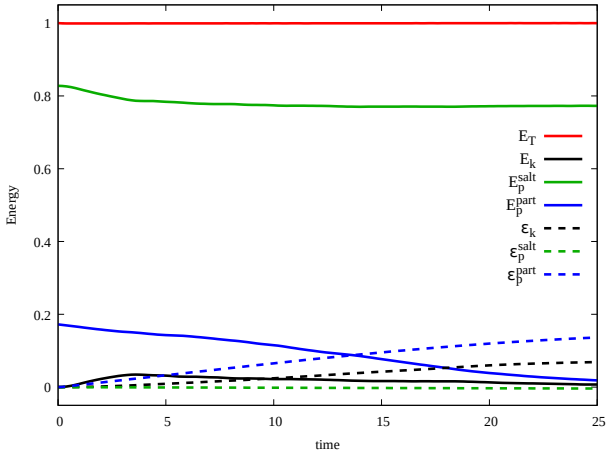

(b) Case #6.2D

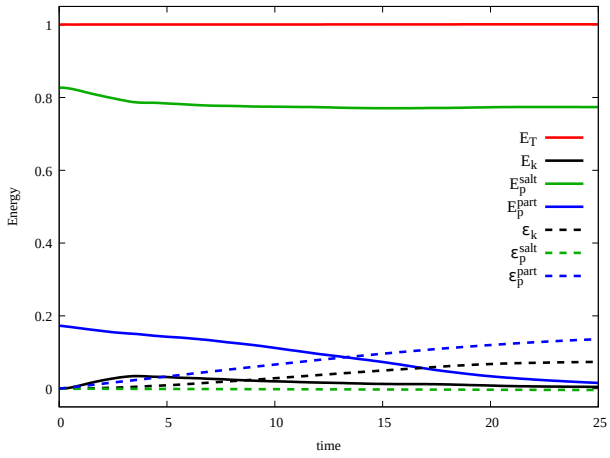

(c) Case #6.3D

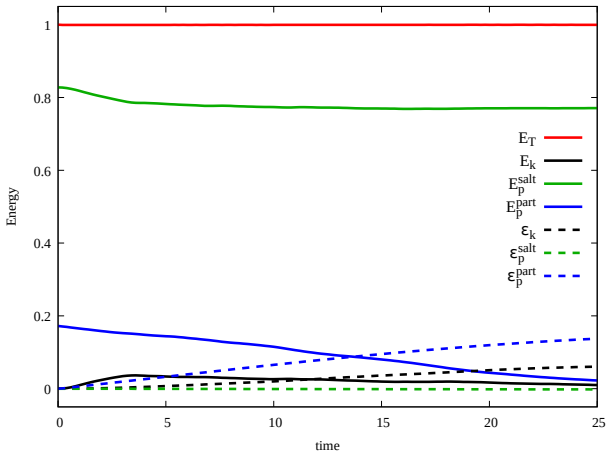

(d) Case #8.2D

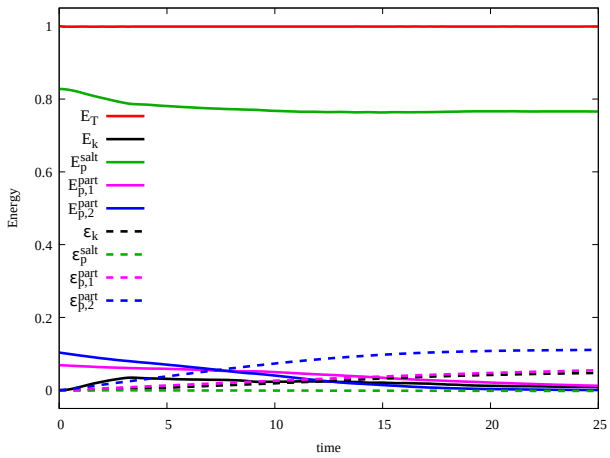

(e) Case #9.2D

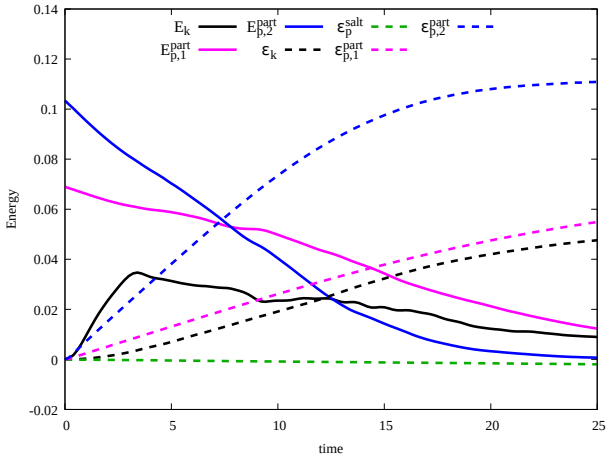

(f) Dissipation detail of case #9.2D

Figure 11: (Color online) Energy evolution in particle-driven cases (a) #5.2D, (b) #6.2D, (c) #6.3D, (d) #8.2D and (e) #9.2D.

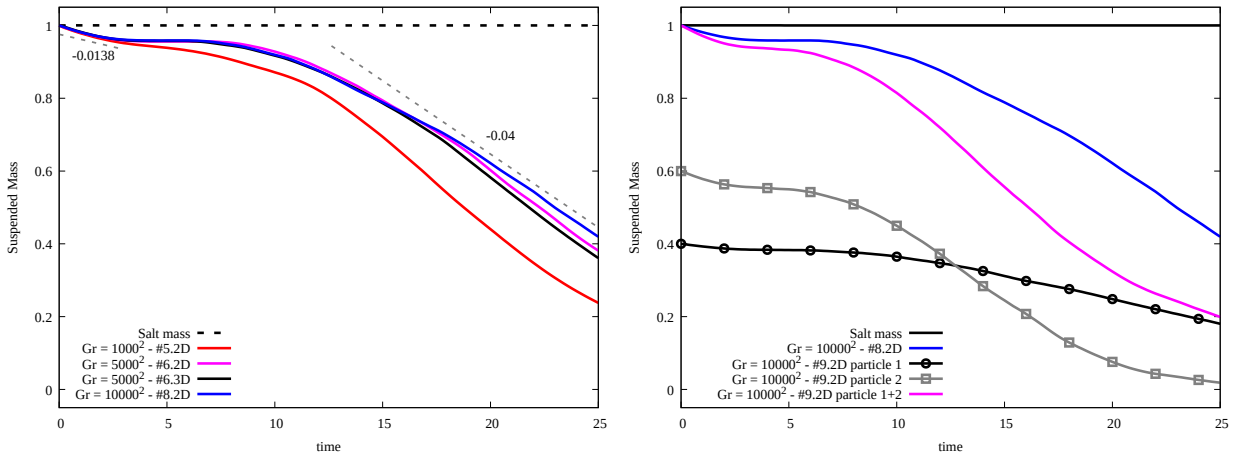

(a) Cases #5.2D, #6.2D, #6.3D, #8.3D, and #9.2D

(b) Cases #8.2D and #9.2D

Figure 12: (Color online) Suspended mass evolution in particle-driven cases. (a) Grashof influence. (b) mono- and bi-disperse cases. All curves are normalized with their respective initial suspended mass m_{p_0}.

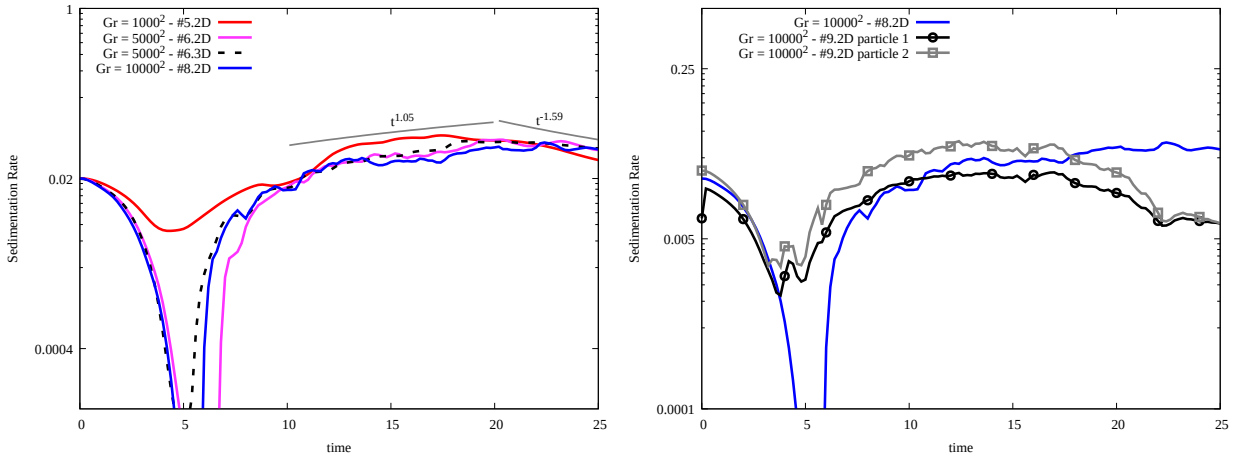

(a) Cases #5.2D, #6.2D, #6.3D, #8.3D, and #9.2D

(b) Cases #8.2D and #9.2D

Figure 13: (Color online) Sedimentation rate evolution in particle-driven cases. (a) Grashof influence. (b) mono- and bi-disperse cases.

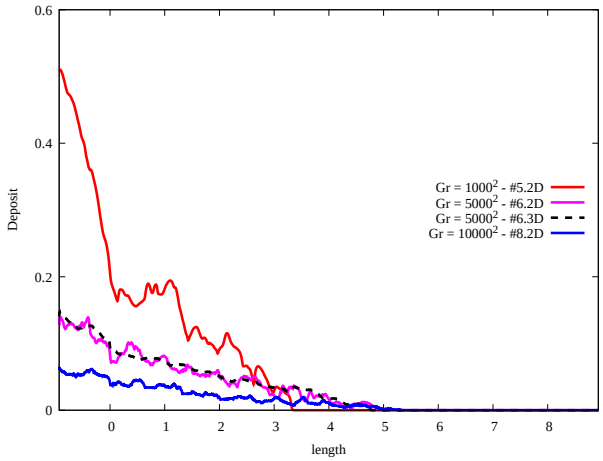

(a) Cases 5.2D, 6.2D, 6.3D and 8.2D

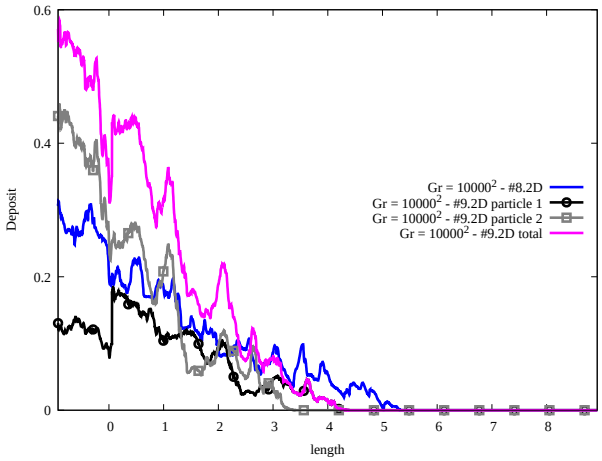

(b) Cases 8.2D and 9.2D

Figure 14: (Color online) Deposit profiles. Figure (a) is normalized by a factor 5×10^{-3}. Figure (b) is normalized by a factor 1×10^{-3}.

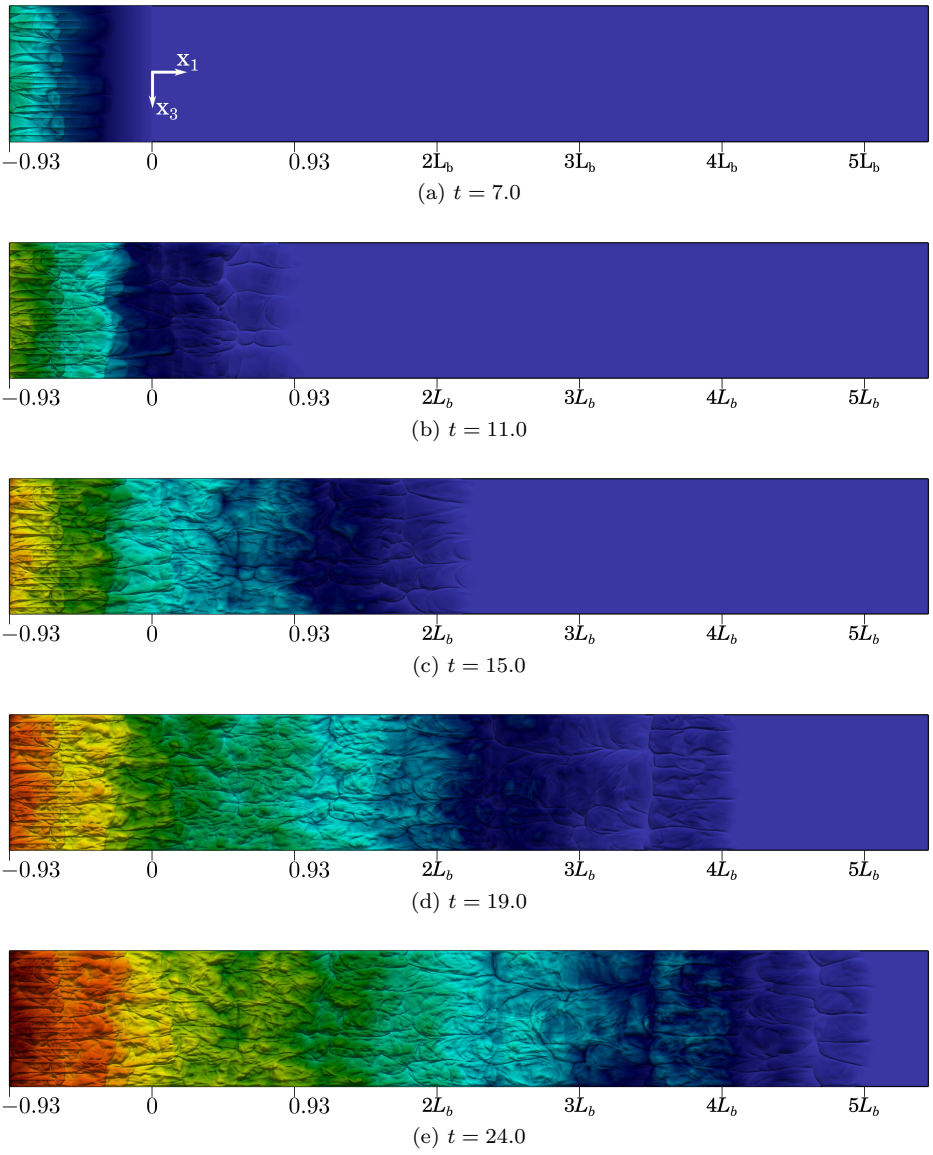

Figure 15: (Color online) Sedimentation map showing the deposit patterns at (a) $t = 7.0$, (b) $t = 11.0$, (c) $t = 15.0$, (d) $t = 19.0$ and (e) $t = 24.0$. Blue corresponds to zero deposition and red to the maximum deposition.

5. Conclusions

In this work, from a theoretical viewpoint, we derived the complete energy budget equation accounting for energy losses due to internal dissipation and the energy exchanges through the boundaries directly from the governing equations for a general class of geophysical flows. We also provided the derivation of consistent boundary conditions. From a numerical viewpoint, we studied density- and particle-driven gravity currents evolving into a stratified medium. Through direct numerical simulations (DNS), we provided highly-resolved numerical solutions to explore the main spatio-temporal flow features. A qualitative analysis showed an interplay between the Kelvin–Helmholtz and fingering instabilities, where both were occurring concomitantly. A nonstandard finger formation took place where fingers intrude in one another due to the Kelvin–Helmholtz vortices.

- There is an overall agreement between our numerical predictions and theoretical and experimental results in the front position in the density-driven cases. The dimensionless front position evolves at a rate (v_f) that equals the Froude number (Fr).
- In the initial condition the parameter β controls the interface thickness; the larger β, the thicker the interface. As we increase the interface from $\beta = 4\pi$ (#2.2D) to 20π (#3.2D), the current speeds up from 0.332 to 0.384, as the Kelvin–Helmholtz structures are dumped, thus reducing the drag. Also, in increasing the Grashof number $Gr = 1000^2, 5000^2, 10000^2$ (#1.2D, #2.2D, #4.2D), the front velocity increases as well, $v_f \approx 0.293, 0.332, 0.338$.
- The kinetic energy increases up to approximately $t = 3$, which coincides with the time it takes to form the current. That is, at $t \approx 3$, the current has the droplet-shape that evolves into the stratified fluid. After the peak, the kinetic energy is dissipated a at nearly constant rate. This dissipation of kinetic energy is much more evident in the particle-driven cases where both the drag and the mass loss due to deposition are dissipating kinetic energy.
- There are three stages related to the dynamics observable in the suspended mass and sedimentation rate. In the first stage, there is mass in contact with the floor inside the lock, until $t \approx 3$ and suspended mass is being deposited. In the second stage, between $t \approx 3$ to 6, the intrusion evolves, nearly all the mass is suspended and there is no sedimentation. In the third stage, for $t > 6$, the settling of particles decrease the suspended mass at an approximately constant rate of sedimentation. The second stage, where no particles are deposit, are less evident for cases $Gr = 1000^2$ (#5.2D) and $Gr = 10000^2$ (#9.2D).
- In poly-disperse solutions, there is a clear suggestion that the finger formation by different particle weight are formed independently.
- In Espath et al. (2015), for hyperpycnal flows, the lobe-and-cleft structures leave their imprint in the sedimentation map, where the clefts coincide with the valleys. This strong correlation found in hyperpycnal flows is weaker; however, visible, in mesopycnal flows due to the more complex dynamics. In the deposit map of our three-dimensional simulation, we observe five to six imprints related to the deposition of the finger structures.

For future works, we aim to explore the full energy budget equations derived herein in more complex configuration. For instance, we plan to exploit the energy budget set of equations where open boundaries may be considered along with the energy exchange across them. A particular interesting phenomenon is the plunging for particle-driven flows on sloping bottom walls (Schuch et al., 2018, 2021).

acknowledgments

This publication was made possible in part by the CSIRO Professorial Chair in Computational Geoscience at Curtin University and the Deep Earth Imaging Enterprise Future Science Platforms of the Commonwealth

Scientific Industrial Research Organisation, CSIRO, of Australia. This project has received funding from the European Union's Horizon 2020 research and innovation programme under the Marie Sklodowska-Curie grant agreement No 777778 (MATHROCKS). The Curtin Corrosion Centre and the Curtin Institute for Computation kindly provide ongoing support. Additionally, this work was conducted using resources and services at the Visualization Core Lab at King Abdullah University of Science and Technology (KAUST).

Data Availability Statement

Data sharing is not applicable to this article as no new data were created or analyzed in this study.

References

An, S., Julien, P., Venayagamoorthy, S., 2012. Numerical simulation of particle-driven gravity currents. Environmental fluid mechanics 12, 495–513.

Bartholomew, P., Deskos, G., Frantz, R.A., Schuch, F.N., Lamballais, E., Laizet, S., 2020. Xcompact3d: An open-source framework for solving turbulence problems on a cartesian mesh. SoftwareX 12, 100550.

Biegert, E., Vowinckel, B., Ouillon, R., Meiburg, E., 2017. High-resolution simulations of turbidity currents. Progress in Earth and Planetary Science 4, 33.

Burns, P., Meiburg, E., 2015. Sediment-laden fresh water above salt water: nonlinear simulations. Journal of Fluid Mechanics 762, 156–195.

Cheong, H.B., Kuenen, J., Linden, P., 2006. The front speed of intrusive gravity currents. Journal of Fluid Mechanics 552, 1–11.

Espath, L.F.R., Pinto, L.C., Laizet, S., Silvestrini, J.H., 2014. Two- and three-dimensional direct numerical simulation of particle-laden gravity currents. Computers & Geosciences 63, 9–16.

Espath, L.F.R., Pinto, L.C., Laizet, S., Silvestrini, J.H., 2015. High-fidelity simulations of the lobe-and-cleft structures and the deposition map in particle-driven gravity currents. Physics of Fluids (1994-present) 27, 056604.

Espath, L.F.R., Sarmiento, A.F., Vignal, P., Varga, B.O.N., Cortes, A.M.A., Dalcin, L., Calo, V.M., 2016. Energy exchange analysis in droplet dynamics via the Navier–Stokes–Cahn–Hilliard model. Journal of Fluid Mechanics 797, 389–430.

Farenzena, B.A., Silvestrini, J.H., 2017. Linear stability analysis of particle-laden hypopycnal plumes. Physics of Fluids 29, 124102.

Flynn, M., Ungarish, M., Tan, A., 2012. Gravity currents in a two-layer stratified ambient: The theory for the steady-state (front condition) and lock-released flows, and experimental confirmations. Physics of Fluids 24, 026601.

Francisco, E.P., Espath, L., Silvestrini, J., 2018. Direct numerical simulation of bi-disperse particle-laden gravity currents in the channel configuration. Applied Mathematical Modelling .

Frantz, R.A., Deskos, G., Laizet, S., Silvestrini, J.H., 2021. High-fidelity simulations of gravity currents using a high-order finite-difference spectral vanishing viscosity approach. Computers & Fluids 221, 104902.

He, Z., Zhao, L., Chen, J., Yu, C.H., Meiburg, E., 2021. Particle-laden gravity currents interacting with stratified ambient water using direct numerical simulations. Environmental Earth Sciences 80, 80:732.

Julien, P.Y., 1998. Erosion and Sedimentation. 1^{st} ed., Cambridge University Press.

Julien, P.Y., 2010. Erosion and Sedimentation. 2^{nd} ed., Cambridge University Press.

Khodkar, M., Nasr-Azadani, M., Meiburg, E., 2018. Gravity currents propagating into two-layer stratified fluids: vorticity-based models. Journal of Fluid Mechanics 844, 994–1025.

Khodkar, M.A., Nasr-Azadani, M., Meiburg, E., 2016. Intrusive gravity currents propagating into two-layer stratified ambients: Vorticity modeling. Physical Review Fluids 1, 044302.

Laizet, S., Lamballais, E., 2009. High-order compact schemes for incompressible flows: A simple and efficient method with quasi-spectral accuracy. Journal of Computational Physics 228, 5989–6015.

Laizet, S., Li, N., 2011. Incompact3d: A powerful tool to tackle turbulence problems with up to $o(10^5)$ computational cores. International Journal for Numerical Methods in Fluids 67, 1735–1757.

Lowe, R., Linden, P., Rottman, J., 2002. A laboratory study of the velocity structure in an intrusive gravity current. Journal of Fluid Mechanics 456, 33–48.

Monaghan, J.J., 2007. Gravity current interaction with interfaces. Annu. Rev. Fluid Mech. 39, 245–261.

Necker, F., Härtel, C., Kleiser, L., Meiburg, E., 2005. Mixing and dissipation in particle-driven gravity currents. Journal of Fluid Mechanics 545, 339–372.

Nokes, R.I., Davidson, M.J., Stepien, C.A., Veale, W.B., Oliver, R.L., 2008. The front condition for intrusive gravity currents. Journal of hydraulic research 46, 788–801.

Ooi, S., Constantinescu, G., Weber, L., 2007. A numerical study of intrusive compositional gravity currents. Physics of Fluids (1994-present) 19, 076602.

Rooij, F.D., Linden, P., Dalziel, S., 1999. Saline and particle-driven interfacial intrusions. Journal of Fluid Mechanics 389, 303–334.

Schuch, F.N., Meiburg, E., Silvestrini, J.H., 2021. Plunging criterion for particle-laden flows over sloping bottoms: Three-dimensional turbulence-resolving simulations. Computers & Geosciences 156, 104880.

Schuch, F.N., Pinto, L.C., Silvestrini, J.H., Laizet, S., 2018. Three-dimensional turbulence-resolving simulations of the plunge phenomenon in a tilted channel. Journal of Geophysical Research: Oceans 123, 4820–4832.
Sutherland, B., Kyba, P., Flynn, M., 2004. Intrusive gravity currents in two-layer fluids. Journal of Fluid Mechanics 514, 327–353.
Sutherland, B.R., Gingras, M.K., Knudson, C., Steverango, L., Surma, C., 2018. Particle-bearing currents in uniform density and two-layer fluids. Phys. Rev. Fluids 3, 023801.
Sutherland, B.R., Nault, J.T., 2007. Intrusive gravity currents propagating along thin and thick interfaces. Journal of Fluid Mechanics 586, 109–118.
Tan, A., Nobes, D., Fleck, B., Flynn, M., 2011. Gravity currents in two-layer stratified media. Environmental fluid mechanics 11, 203–223.
Ungarish, M., 2005. Intrusive gravity currents in a stratified ambient: shallow-water theory and numerical results. Journal of Fluid Mechanics 535, 287–323.
Ungarish, M., 2009. An introduction to gravity currents and intrusions. CRC press.
White, B.L., Helfrich, K.R., 2012. A general description of a gravity current front propagating in a two-layer stratified fluid. Journal of Fluid Mechanics 711, 545–575.